

A Model for Self-Support Evaluation of 3D-Printed Structures with Inclined Surfaces

by

Taylor Sweet

A thesis submitted in partial fulfilment of the requirements for
the degree of

Master of Applied Science

in

The Faculty of Graduate and Postdoctoral Studies
(Mechanical Engineering)

The University of British Columbia
(Vancouver)

December 2019

© Taylor Sweet, 2019

The following individuals certify that they have read, and recommend to the Faculty of Graduate and Postdoctoral Studies for acceptance, a thesis entitled:

A Model for Self-Support Evaluation of 3-D Printed Structures with Inclined Surfaces

submitted by Taylor Mackenzie Sweet in partial fulfillment of the requirements for the degree of Master of Applied Science in Mechanical Engineering

Examining Committee:

Dr. Hsi-Yung (Steve) Feng

Supervisor

Dr. Yusuf Altintas

Supervisory Committee Member

Dr. Mu Chiao

Supervisory Committee Member

Abstract

Additive manufacturing (AM) is renowned for its flexibility and low upfront costs. Amongst the variety of AM technologies, fused filament fabrication (FFF) is by far the most prevalent [1]. FFF printers work by extruding molten polymer in a series of planar layers according to directions derived from computer-aided design (CAD) data. While FFF provides a low-cost alternative to conventional manufacturing for small-batch prototyping, it's hindered by its time-intensive nature and high unit cost of production. One contributing factor to the manufacturing time and material costs of FFF is the requirement to print additional supporting structures in order to facilitate the construction of inclined surfaces. In absence of these structures, the forces acting on the unsupported (overhanging) portion of the molten extrusions are liable to cause deformation or collapse. As per the universally-quoted heuristic, any surface that is inclined by more than 45° from the vertical should be supported. However, to date, there has been little justification provided to support this heuristic and, in fact, components with surface angles exceeding 45° are routinely produced without support using FFF printers. In this work we present a theory to explain the limiting phenomena in the printing of inclined surfaces via FFF. We also develop a model to predict a component's printability based on its geometry, the process parameters and the material properties of the filament. Experimental validation is provided to verify the appropriateness of the model. The results indicate that the phenomena limiting the maximum surface angle are scale-dependent. For large-scale FFF printing, the angle is limited by gravity, which tends to cause the extruded filament to deflect downwards, limiting the vertical progression of the structure. For small-scale printing, the angle is limited by surface tension, which tends to cause the extruded filament to contract, limiting the structure's horizontal progression. At small scales the maximum surface angle was found to depend solely on the geometry of the print bead and the number of perimeters, whereas at large scales it also depends on the process parameters and

material properties.

Lay Summary

This paper presents a theory that explains the limiting phenomena in the manufacture of structures with inclined surfaces via fused filament fabrication 3-D printing. Based on this theory, a model is developed for prediction of the maximum printable surface angle according to the layer geometry, process parameters and material properties. The results of a series of experiments are then presented as a means of verifying the model accuracy.

Preface

This thesis is original, unpublished, independent work by the author, T. Sweet.

Table of Contents

| | |
|--|-------------|
| Abstract | iii |
| Lay Summary | v |
| Preface | vi |
| Table of Contents | vii |
| List of Tables | ix |
| Table of Figures | x |
| Acknowledgments | xiii |
| Dedication | xiv |
| 1 Introduction | 1 |
| 1.1 Motivation | 5 |
| 1.2 Literature Review | 7 |
| 1.3 Objectives and Organization | 14 |
| 1.4 Background | 14 |
| 2 Theory | 17 |
| 2.1 Definitions | 17 |
| 2.1.1 Print Bead Geometry and Overhang Angle | 17 |
| 2.1.2 Limiting Phenomena | 19 |

| | | |
|----------|--|-----------|
| 2.1.3 | Process Timescales | 21 |
| 2.2 | Failure Modes | 22 |
| 2.2.1 | Prevalence of Sag and Shrink | 22 |
| 2.2.2 | Sag | 26 |
| 2.2.3 | Shrink | 28 |
| 2.3 | Multiple Perimeters | 37 |
| 3 | Model | 39 |
| 3.1 | Sag – Large-scale FFF | 39 |
| 3.1.1 | Solidification | 41 |
| 3.1.2 | Print Bead Dynamics | 44 |
| 3.1.3 | Implementation | 48 |
| 3.1.4 | Integration | 48 |
| 3.1.5 | Results | 50 |
| 3.2 | Shrink – Small-scale FFF | 53 |
| 3.2.1 | Assumptions | 53 |
| 3.2.2 | Derivation | 54 |
| 3.2.3 | Multiple Perimeters | 58 |
| 3.2.4 | Implementation | 59 |
| 3.2.5 | Results | 60 |
| 4 | Experimental Validation | 65 |
| 4.1 | Single Perimeter | 66 |
| 4.2 | Multiple Perimeters | 72 |
| 5 | Results and Discussion | 74 |
| 5.1 | Conclusions and Future Work | 75 |

List of Tables

| | | |
|-----|--|----|
| 1.1 | Additive manufacturing technology descriptions | 2 |
| 1.2 | Additive manufacturing technology support requirements . . . | 5 |
| 4.1 | Experimental setup | 65 |

List of Figures

| | | |
|------|---|----|
| 1.1 | Support type examples | 4 |
| 1.2 | Example of soluble (left) and non-soluble (right) support structures. | 6 |
| 1.3 | Visual depiction of the 45° rule. | 12 |
| 1.4 | Overhang angle test object print result. | 13 |
| 1.5 | Layer height comparison. | 14 |
| 1.6 | Printer comparison. Left: desktop FDM printer (scale: 1:10); Right: BAAM printer (scale: 1:150). | 15 |
| 2.1 | Archway example illustration. | 18 |
| 2.2 | Overhang angle illustration. | 18 |
| 2.3 | Print bead geometry definition and layer stacking illustration. | 19 |
| 2.4 | Overhang comparison. | 20 |
| 2.5 | Sag/shrink illustration. | 20 |
| 2.6 | Scale comparison of FFF applications | 24 |
| 2.7 | Visualization of the prevalence of sag and shrink. | 26 |
| 2.8 | Illustration of cumulative sag in stacked layers. | 27 |
| 2.9 | Illustration of cumulative shrink in stacked layers. | 29 |
| 2.10 | Cross-sectional view of overhang feature illustrating evolution of bead geometry due to shrink. | 31 |
| 2.11 | Droop illustration for $h = 300 \mu m$ and $\theta = 50^\circ$ | 31 |
| 2.12 | Droop illustration for $h = 300 \mu m$ and $\theta = 56^\circ$ | 32 |
| 2.13 | Droop reference and comparison. | 32 |

| | | |
|------|--|----|
| 2.14 | Reference geometry and print result for inverted cone with $h = 300 \mu m$ and $\theta = 50^\circ$ | 33 |
| 2.15 | Illustration of nozzle-structure offset deviation for inverted cone geometry. | 34 |
| 2.16 | Illustration of nozzle-structure offset deviation for inverted pyramid geometry. | 35 |
| 2.17 | Reference geometry and print result for inverted pyramid with $h = 300 \mu m$ and $\theta = 56^\circ$ | 36 |
| 2.18 | Contact area comparison for different print regimes (bead geometries). | 36 |
| 2.19 | Illustration of infill percentage and number of shells | 37 |
| 3.1 | Print bead geometry and slice definition. | 40 |
| 3.2 | Slice force diagram. | 40 |
| 3.3 | Sag model progress example. | 49 |
| 3.4 | Sag model results for a scale factor of 50. | 51 |
| 3.5 | Sag model results for a scale factor of 100. | 52 |
| 3.6 | Viscosity versus shear rate for PLA. | 55 |
| 3.7 | Print bead geometry evolution due to shrink. | 56 |
| 3.8 | Shrink percentage versus overhang angle. | 57 |
| 3.9 | Shrink model results for $h = 150 \mu m$ | 61 |
| 3.10 | Shrink model results for $h = 300 \mu m$ | 62 |
| 3.11 | Left: layer progression with variable overhang angle; Right: bead width v.s. overhang offset. | 62 |
| 3.12 | Left: layer progression with variable overhang angle and two perimeters; Right: bead width v.s. overhang offset. | 63 |
| 3.13 | Layer progression for $h = 150 \mu m$, $\theta = 60^\circ$ and 2 perimeters. | 63 |
| 3.14 | Layer progression for $h = 150 \mu m$, $\theta = 69.5^\circ$ and 2 perimeters. | 64 |
| 3.15 | Layer progression for $h = 150 \mu m$, $\theta = 75^\circ$ and 2 perimeters. | 64 |
| 4.1 | Test object geometry. | 66 |

| | | |
|------|---|----|
| 4.2 | Results comparison for $h = 150 \mu m$ and $\theta = 50^\circ$ | 67 |
| 4.3 | Results comparison for $h = 150 \mu m$ and $\theta = 55^\circ$ | 68 |
| 4.4 | Results comparison for $h = 150 \mu m$ and $\theta = 60^\circ$ | 68 |
| 4.5 | Results comparison for $h = 150 \mu m$ and $\theta = 65^\circ$ | 69 |
| 4.6 | Results comparison for $h = 300 \mu m$ and $\theta = 30^\circ$ | 69 |
| 4.7 | Results comparison for $h = 300 \mu m$ and $\theta = 40^\circ$ | 70 |
| 4.8 | Results comparison for $h = 300 \mu m$ and $\theta = 45^\circ$ | 70 |
| 4.9 | Results comparison for $h = 300 \mu m$ and $\theta = 50^\circ$ | 71 |
| 4.10 | Results comparison for $h = 300 \mu m$ and $\theta = 45^\circ$ with 2 perimeters | 72 |
| 4.11 | Results comparison for $h = 300 \mu m$ and $\theta = 56^\circ$ with 2 perimeters | 73 |
| 4.12 | Results comparison for $h = 300 \mu m$ and $\theta = 68^\circ$ with 2 perimeters | 73 |

Acknowledgments

Many thanks to Dr. Hsi-Yung (Steve) Feng for his guidance and support.

My sincere gratitude to the National Science and Engineering Research Council of Canada (NSERC) for their funding of this research.

Thank you to my parents for their love and encouragement.

To my fiancé, Erin, thanks for coming along for the ride.

To Erin

Chapter 1

Introduction

Additive manufacturing (AM), colloquially known as 3-D printing, is a manufacturing technique which uses computer-aided design (CAD) data to construct a component layer by layer through the sequential addition of material. According to the joint standard developed by the International Organization for Standardization (ISO) and the American Society for Testing and Materials (ASTM), 3-D printing technologies can be broadly categorized into 1 of 7 distinct groups [2]. These groups and a brief description of each are provided in Table 1.1.

While the approaches to 3-D printing vary widely, one thing that is nearly ubiquitous is the reliance on supporting structures to help facilitate the process. Depending on the technology, these structures take different forms and serve different functional purposes. In the case of technologies that impose high thermal gradients, such as selective laser melting, support structures help to dissipate heat and increase rigidity, protecting against distortion from residual stresses [3]. In material extrusion technologies, such as fused filament fabrication, support structures help resist deformation or collapse resulting from unbalanced forces on the molten material. Such structures are employed wherever successive layers are significantly offset (overhanging), which is a

Table 1.1: Additive manufacturing technology descriptions [2]

| Technology | Description |
|----------------------------|---|
| Binder Jetting | a liquid bonding agent is selectively deposited to join powder materials |
| Directed Energy Deposition | focused thermal energy is used to fuse materials by melting as they are being deposited |
| Material Extrusion | material is selectively dispensed through a nozzle or orifice |
| Material Jetting | droplets of build material are selectively deposited |
| Powder Bed Fusion | thermal energy selectively fuses regions of a powder bed |
| Sheet Lamination | sheets of material are bonded to form a part |
| Vat Photopolymerization | liquid photopolymer in a vat is selectively cured by light-activated polymerization |

requirement for the construction of inclined surfaces. Support structures are also universally used as fixtures in the case where the model is unbalanced or elements of the geometry are not initially connected to the bulk structure.

For ease of reference, we classify supports as belonging to one or more of three functional groups: 1. Thermal, 2. Overhang and 3. Fixture. Consider, for instance, selective laser melting (SLM), which uses a high power-density laser to melt and fuse metallic powders [4]. In this case, supporting structures may be employed for one or both of two reasons: thermal dissipation and fixturing [5]. Since SLM is a powder bed technique, the role of overhang support is played by the raw material. That is, the virgin powder acts to support the molten layers as they cool. Thus, SLM does not require additional supporting structures in order to enable the printing of surfaces with extreme inclines or overhangs. However, despite benefiting from the inherent support of the virgin powder, components manufactured via SLM may still require fixture supports. This is because of the action of the recoater, which wipes over the component after the completion of each layer to deposit new powder. If there are any disconnected geometrical elements this may inadvertently cause them to shift relative to one another [6]. Thus, fixture supports are employed to anchor these elements and prevent them from shifting. Figure 1.1 gives an example of each of the three different categories of support.

Selective laser sintering (SLS) is very similar to SLM, with the essential difference being the binding method that occurs between the powder particles [7]. In SLM the powder is heated until it is fully molten, while in SLS the powder is only heated until it is partially molten and just begins to coalesce. The result is that there is less thermal energy to be dissipated and therefore thermal supports are much less likely to be necessary [3]. Moreover, SLS, like SLM, benefits from the presence of the virgin powder, rendering overhang

supports unnecessary. Thus, the only type of support required for SLS is that for fixturing.

Another 3-D printing technology which relies heavily on support structures is stereolithography (SLA), an example of vat photopolymerization. In this technique a light source is used to cure a liquid photosensitive polymer in a layer-wise manner [8]. In most SLA printers the build platform is downward facing (surface normal aligned with gravity vector), meaning that the component is inverted during the print process. For this reason fixture supports are used extensively in almost all cases to prevent the print from detaching from the build surface under the influence of gravity [9].

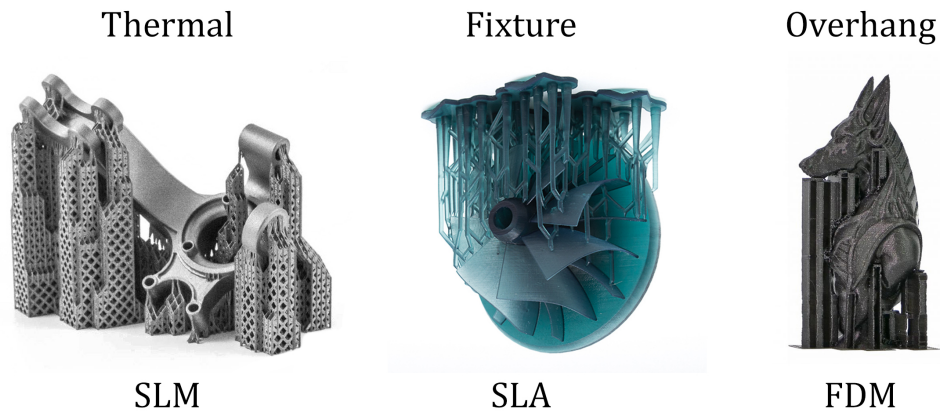


Figure 1.1: Support type examples [10][11][12]

Amongst the variety of AM technologies, fused filament fabrication (FFF), also known under the trademarked term fused deposition modeling (FDM), is by far the most prevalent [1]. This technology falls under the category of material extrusion, which utilizes support types 2 and 3: overhang and

fixture. Overhang supports are necessary because, in the case of inclined features, the unsupported (overhanging) portions of the perimeter extrusions are prone to deformation and collapse as a result of the forces acting on the molten material. Since the working material is plastic and not metal, the temperatures are comparatively low and thermal supports are not required. Table 1.2 provides a summary of the various 3-D printing technologies and the relevant supporting structures for each.

Table 1.2: Additive manufacturing technology support requirements

| Technology | Example | Support Type |
|----------------------------|---|---------------------|
| Binder Jetting | | 3 |
| Directed Energy Deposition | | 1,2,3 |
| Material Extrusion | Fused Filament Fabrication (FFF) | 2,3 |
| Material Jetting | | 2,3 |
| Powder Bed Fusion | Selective Laser Melting/Sintering (SLM/SLS) | 1,3 |
| Sheet Lamination | | - |
| Vat Photopolymerization | Stereolithography (SLA) | 2,3 |

1.1 Motivation

Regardless of the function of the supporting structures, printing them will incur additional manufacturing time and material costs. By default, the support will be printed using the same material as the model. With many

methods, including powder bed fusion, binder jetting, and vat photopolymerization, this is generally the only option. Material extrusion is unique in that it is possible to print with multiple materials, either through the use of dual extruders or a multi-filament feed system. This enables the use of soluble supports which are trivial to remove. On the other hand, when supports are metallic, as in SLM/SLS, removing them requires extensive post-processing. Figure 1.2 illustrates the different types of support in FFF.

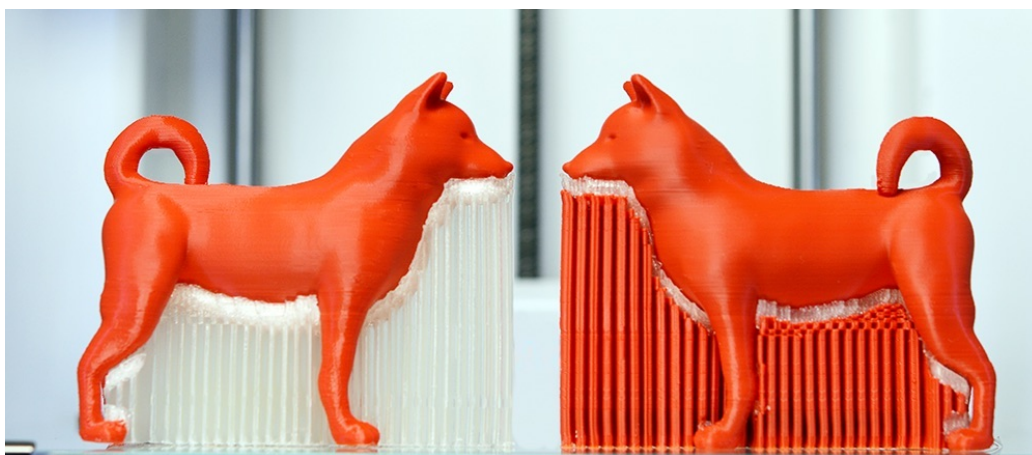


Figure 1.2: Example of soluble (left) and non-soluble (right) support structures [13].

While material extrusion methods benefit from the least costly and easiest to remove support structures, printing them still incurs additional print time and soluble filament comes at a premium. Furthermore, depending on the geometry, it may not be possible to remove the supports whatsoever. Such is the case wherever an internal facet of the geometry requires support, in which case supports will be rendered inaccessible upon the completion of printing and thus are unable to be removed.

Due to the inherent drawbacks of support structures, it is desirable to reduce the extent of their use wherever possible. To this end, many researchers have devoted their time to studying support structures and their optimization, particularly as it pertains to fused filament fabrication. Unfortunately, there is a lack of consensus on the critical overhang angle for support generation, which is an important input to the optimization efforts.

1.2 Literature Review

Among the simplest approaches to support volume reduction for FFF is part orientation optimization, an example of which is provided by Das et al [14]. In this work a voxel-based approach is employed to calculate the support structure requirement as a function of build orientation. By optimally orienting the component the extent of support structure requirement can be kept to a minimum. In this work the surface angle threshold for support generation is set at 45° .

A different approach to reducing the volume of support is to optimize its distribution. Such an approach was taken by Jin et al. [15]. In an effort to avoid the difficulties associated with handling three-dimensional data they propose a support generation algorithm based on sliced layers. With a given threshold value of the surface inclination angle, all the possible support configurations are evaluated by computing the distance between points on adjacent layers. In this work a threshold angle of 78° was selected.

Yet another strategy to reduce the volume of support is to optimize its topology rather than its distribution. Such an approach was taken by Strano et al. [16] in their 2013 work titled, “A new approach to the design and optimisation of support structures in additive manufacturing”. Their efforts centered around the concept of cellular support structures defined using a

mathematical formulation of 3-D implicit functions. This enabled them to generate graded structures that provide more robust support where the component’s weight concentrates and save material elsewhere. Their results indicate a material savings of as much as 50% with their topology-optimized support structures. The facets that needed to be supported were determined based on a threshold value of the inclination angle. They state that “the threshold value of 85° was chosen arbitrarily, in order to emphasize the support structure”.

In their 2014 paper titled “Clever Support: Efficient Support Structure Generation for Digital Fabrication”, Vanek et al. [17] took a hybrid approach by optimizing the model orientation as well as the support topology and distribution. Their strategy was to first detect the points that require support and then to progressively generate the support structure, attempting to minimize its overall length at every step. The result is a tree-like branching structure that effectively supports all overhangs while achieving material and print time reductions in the neighborhood of 40% and 30%, respectively. In reference to the overhang threshold, the researchers state that “most FDM printers are capable of printing faces deviating by up to 45° from the printing direction vector” and that “the exact value of the [critical overhang angle] varies from printer to printer and is not generally accessible.”

Perhaps the best approach to reduce support requirements is to design the component structure such that they are not required. A self-supporting structure is one that does not necessitate the use of supplementary support material during the build process [18]. In their 2017 work, Guo et al. [19] used the moving morphable voids framework for explicit topology optimization of the component as a whole, imposing a self-support constraint to ensure the resulting geometry could be manufactured without supports. This constraint was derived from the understanding that “the overhang angle is material and

process dependent” and that “the commonly accepted value of the maximum overhang angle amounts to $40^\circ - 50^\circ$.”

In FFF, overhang supports are typically only required external to the component, in regions where the geometry has steeply inclined surfaces (overhangs). Internally, the surfaces are typically all well supported by the solid infill which is used to give a component its rigidity. However, in recent years, many researchers have devoted their attention to optimizing the interior distribution of material with objectives including material reduction and uniform stress distribution under specified loads [20][21]. While this optimized infill serves to increase the strength to weight ratio of the component it introduces a problem. Previously, support structures were only ever required externally, but now they may also be required internally, depending on the configuration of the infill.

While exterior support structures can be removed in post-processing, interior supports cannot. Thus, if the infill necessitates their use in order to ensure the printability of the component, the benefits of the optimization are effectively negated. Therefore, the inclusion of an overhang angle constraint is essential to the optimization.

A multitude of researchers have proposed different methods for the generation of optimized infill structures. Prévost et al. [22] set out to ensure static stability by formulating balance optimization as an energy minimization problem and using this to inform the distribution of material in the interior of the part. While effective at accomplishing the stability objective, they did not include an overhang angle constraint and thus the self-support property of the resulting structure, and by extension the printability, is not ensured.

Xie et al. [23] improved on the work of Prévost et al. by optimizing for both static and dynamic (rotational) stability. They employed a method called interior carving which is the process of hollowing voids inside an object without affecting its outward appearance. More importantly, they included an overhang angle constraint to ensure self-support of the resulting structure. They claim that with “sufficiently small [overhang angle], α (we fix $\alpha = 30^\circ$), the structure is safe to print without supporting structures.”

Lee and Lee, in their papers on block-based inner support generation [24][25], focused strictly on a material reduction objective. In this approach, three-dimensional block-based partitioning is used to segment a volume. The blocks are iteratively subdivided until all “flat roof” regions are supported. Since the unit block is defined in such a way as to be self-supporting (angle between positive z axis and each face normal is larger than a given threshold), the global interior structure will inherently adopt this property. They purport that “in general, when the layered angle is greater than 45° , the object can be stacked in a stable manner.”

On the topic of load-informed infill generation, Wang et al. proposed a skin-frame structural optimization approach that utilized a truss lattice support structure [21]. In this framework, the design variables were the positions of the nodes and the radii of each of the truss elements, while the outer shell or “skin” was assigned a fixed width and not optimized. The loading conditions were incorporated by using finite element analysis to determine the deformation of the surface nodes. A similar work produced by an overlapping group of contributors optimized for global compliance minimization (stiffness maximization) instead of a specified loading condition [26]. Unfortunately, due to the absence of an overhang constraint in either of these works, the printability of the resulting structures is not ensured.

Numerous other researchers have proposed optimized infill structures without ensuring printability. For instance, Zhang et al. [27], who also employed a truss lattice support structure but developed it using the concept of the medial-axis tree, and Lu et al. [28] who developed a hollowing algorithm modeled on a honeycomb cell. The former suffers from the same printability concerns as the skin-frame structure of Wang et. al., which is a result of the extreme overhangs inherent in the unstructured truss lattice. In the case of the latter, while a self-support constraint wasn't strictly imposed, the honeycomb structure inherently has fewer and less extreme overhangs and thus, while the printability is not ensured, the resulting structures are often still printable. However, depending on the scale of the honeycomb cells, the flat roof regions that they create may be prone to collapse. Thus, the optimized structures are not universally printable.

While no overhang constraint is strictly enforced, in their paper on bone-like porous infill, Wu et al. [29] claim that this type of infill “has small overhang in general and thus naturally satisfies manufacturability constraints without the need for additional supporting material.” In a separate paper produced by Wu et al. [30] they propose a different infill structure based on the rhombus which is self-supporting by design. In their own words “a rhombic shell is said to be self-supporting if it can be fabricated without adding support structures in the cavity.” They go on to say that “the allowed maximum angle of overhangs is a device-dependent parameter taking different values depending on the used 3D printers.”

Regardless of the approach of the aforementioned works or whether they focused on optimizing internal supports or external supports, they have a commonality: a dependence on knowledge of the critical overhang angle. Those works that incorporated an explicit overhang angle threshold were able to ensure the printability of the resulting structures, while those that

didn't, were not. The difficulty is that this threshold is not universally agreed upon and, as Vanek et al. [17] pointed out, it “varies from printer to printer and is not generally accessible”. Most commonly, the critical overhang angle is quoted as 45° . This is illustrated in Figure 1.3.



Figure 1.3: Visual depiction of the 45° rule [31].

Despite the frequent use of 45° as a threshold for the requirement of support, it is in fact possible to print surfaces that exceed this angle, albeit with varying degrees of success, as evidenced by the test object in Figure 1.4. To date, and to the best of the author’s knowledge, there is no theory that can explain the reasoning behind the 45-degree heuristic, besides most sources claiming that at an overhang angle of 45° the layer-layer contact is reduced to 50% of the extrusion width.

A quote from popular 3-D printing reference site *All3DP* [32] reads: “Usually, overhangs up to 45 degrees can still be printed without loss of quality. That’s because any layer in a 45-degree overhang is 50% supported by the layer beneath. In other words, each new layer has enough support to remain intact and to make printing possible.” While such a justification is often used to support the 45-degree constraint heuristic, it is inherently flawed. This is because the length of the overhang is a function of the layer height. That is,

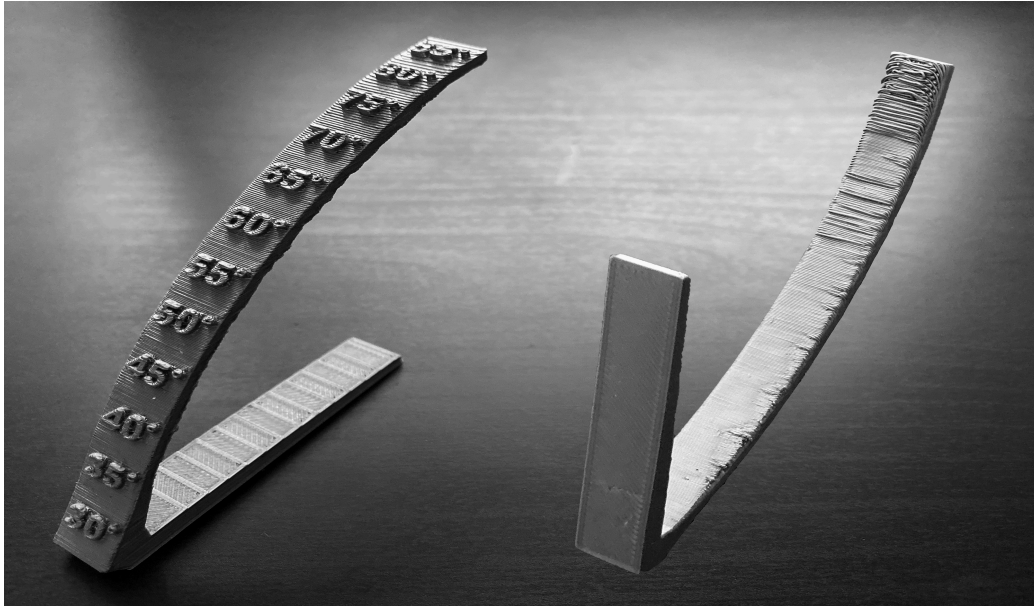


Figure 1.4: Overhang angle test object print result.

the smaller the layer height, the shorter the length of overhang required to achieve the same surface angle. Thus, a 45-degree overhang only corresponds to 50% support if the aspect ratio (width:height) of the extrusion is 2:1. This concept is demonstrated in Figure 1.5, where the extrusion width is $400\ \mu\text{m}$. Note that the layers have 50% support at 45° in the right-hand image, where the aspect ratio is 2:1, while in the left-hand image the supported percentage is closer to 70% with the same surface angle.

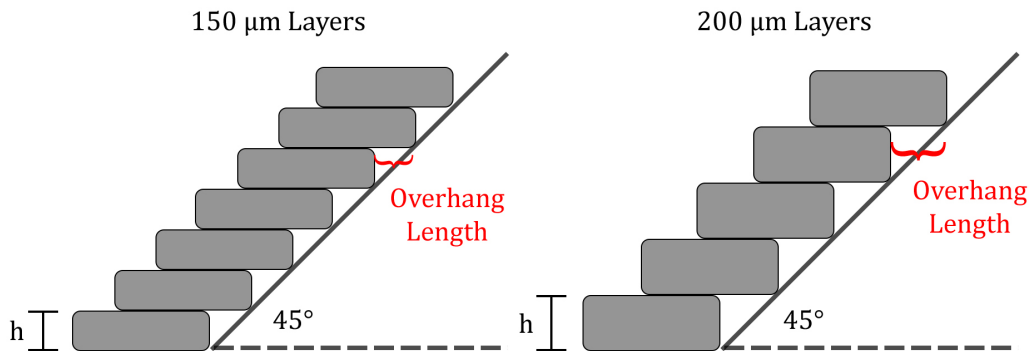


Figure 1.5: Layer height comparison.

1.3 Objectives and Organization

Given the lack of clarity on the overhang angle concept and the heavy reliance on it for support structure optimization efforts, there is evidently room for new research in this area. This work presents a theory that attempts to explain the phenomena limiting the maximum overhang print angle. Based on this theory, we develop a model that can help predict the printability of a candidate structure based on its geometry and the parameters of the process (print settings and material properties). We then provide some examples of the model’s output, including comparisons to experimental results to validate its accuracy. Finally, we conclude by commenting on the model’s limitations and suggest future work that could be done to improve it.

1.4 Background

FFF printers input thermoplastic filament, heat it to its melting point and extrude the molten polymer through a nozzle in a series of planer layers. The position of the nozzle is informed by a sequence of motor control commands (“g-code”), which are generated by a software package called a “slicer”. The slicer takes as input a 3-D model, typically in the form of an STL file, and

a variety of printer configuration parameters, including temperatures and velocities, and outputs the g-code necessary to produce the component.

Typical FFF printers have a build volume on the order of centimeters and a layer height on the order of hundreds of micrometers. However, specialty machines exist which are capable of printing at much larger scales, with build volumes on the order of meters and layer heights on the order of centimeters. These machines are based on the technologies known as Big Area Additive Manufacturing (BAAM) and Large Scale Additive Manufacturing (LSAM) [33]. Figure 1.6 provides a comparison of the two distinct scales of FFF 3-D printers. Regardless of the scale, due to the additive nature of the process and the influence of surface and body forces on the molten extrusions, some features require additional support in order to print successfully.



Figure 1.6: Printer comparison. Left: desktop FDM printer (scale: 1:10) [34]; Right: BAAM printer (scale: 1:150) [33].

While there is no existing research concerning the critical overhang print

angle, a number of works have been presented in the general topic area of process modeling for additive manufacturing. In their publication titled “Physics of 3-D Printing”, Amina Alić [35] provides general insight into the physical phenomena that govern the extrusion and deposition of polymer filaments in FFF. Costa et al. [36] and Balani et al. [37], in their respective works, dig deeper into the rheological properties of the filament and the adhesion development between adjacent strands. Another work, that by Comminal et al. [38], investigated strand morphology evolution on a uniform substrate but omitted consideration of layer stacking.

The most relevant works are those by Xia et al. [39] and Verma et al. [40] which offer computational models and fully-resolved numerical simulations for the FFF process. Unfortunately, none of these works includes consideration of offset strands. That is, the results provided are limited to perfectly vertical surfaces and do not apply to overhangs. While it may be possible to extend these models to include consideration of overhangs, it would be quite computationally expensive to simulate for every layer in a complex structure. Further, the results would still need to be interpreted in order to develop a theory concerning the limiting phenomena in the printing of inclined surfaces.

Chapter 2

Theory

2.1 Definitions

2.1.1 Print Bead Geometry and Overhang Angle

FFF printers construct components in a layer-wise manner by incrementing the vertical distance (z-offset) between the nozzle and print surface upon completion of each layer. As such, each layer is discrete and the total number of layers is finite. In order to achieve a change in the cross-sectional geometry of the component being built, the print strands (material extrusions) at the layer perimeters, in addition to having a vertical offset, must also be offset laterally. This is akin to building an archway with bricks which have finite height and width. In order to bridge the gap between the walls, a subset of the bricks must be horizontally offset from their predecessors, such that the sum of the offsets is equal to the wall separation. This is illustrated in Figure 2.1.

Given the local angle of a perimeter surface in the candidate geometry and the configuration-specified layer height (smaller: slower printing, finer detail; larger: quicker printing, coarser detail), one can determine the neces-

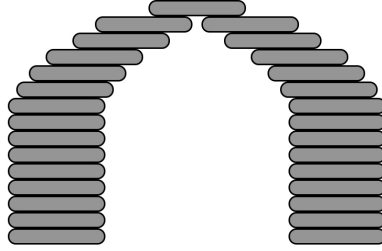


Figure 2.1: Archway example illustration.

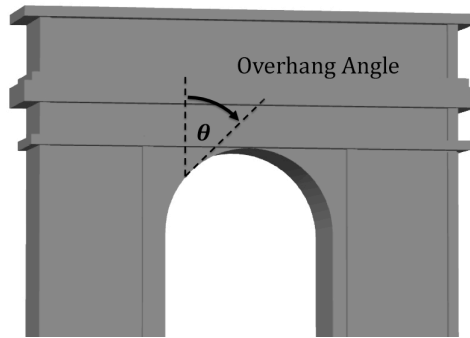


Figure 2.2: Overhang angle illustration.

sary horizontal offset between layers in order to construct the feature. The arctangent of the ratio between horizontal offset and layer height is deemed the overhang angle, θ , which is simply a measure of the local surface angle between adjacent layers. If a surface comprising more than two layers has constant slope, the overhang angles for each pair of adjacent layers will be equal. The overhang angle concept is illustrated in Figure 2.2.

Figure 2.3 provides the print bead geometry definition, where h is the layer height and w is the bead width. This figure also illustrates the stacking of print strands in successive layers, where d_n is the horizontal offset and θ_n is the overhang angle. In this terminology, the print bead is defined as a unit length of the print strand, where the print strand is assumed to be homogeneous over its length at the local instant of deposition. That is, each

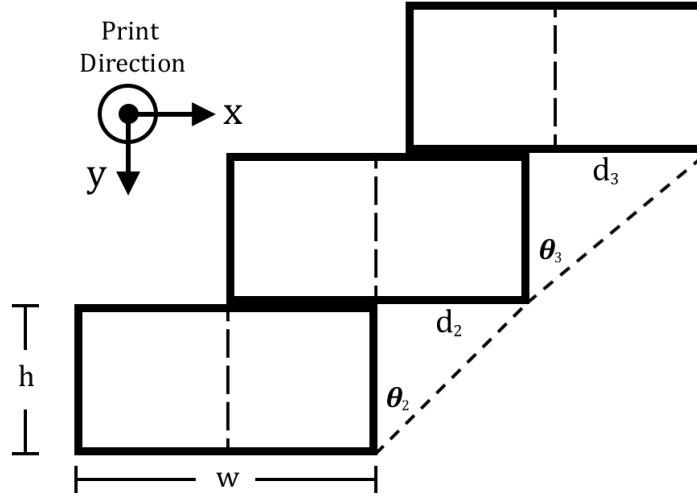


Figure 2.3: Print bead geometry definition and layer stacking illustration.

unit length of extrusion will have the same time evolution and equilibrium position/geometry. In this way, we can simply evaluate the evolution of one print bead and apply the result to the entire strand. Since layer $n = 1$ is on the print bed: $\theta_1, d_1 = 0$. Note also that the print direction is defined to be out of the plane of the page and that, in this example, $\theta_3 > \theta_2$ and thus, by extension, $d_3 > d_2$.

Note: in Figure 2.3 the coordinate axes are defined for future notational convenience and do not coincide with the printer's build volume.

2.1.2 Limiting Phenomena

For a given layer height a steeper surface slope (larger overhang angle) necessitates a larger horizontal offset between layers, which in-turn means that a bigger percentage of the perimeter print strand in each layer is unsupported versus supported, as depicted by the red line in Figure 2.4. As the percentage of the strand that is unsupported increases with increasing overhang angle,

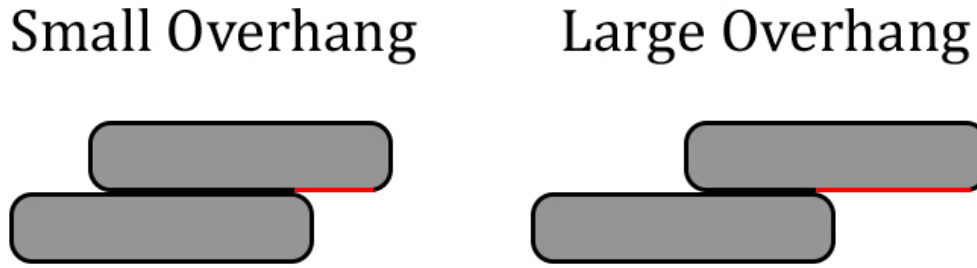


Figure 2.4: Overhang comparison.

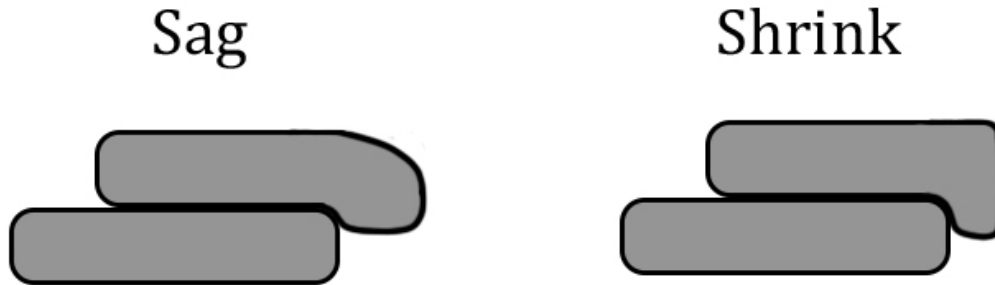


Figure 2.5: Sag/shrink illustration.

by extension, so too will the amount of cantilevered mass. Without the supporting force of the layer below, the cantilevered portion of the extrusion may be subject to an unbalanced gravitational force. This can result in the bead deflecting downwards under its own weight, a phenomena hereafter referred to as “sag”. However, another effect which must be considered is that of surface tension. If the surface forces exceed the gravitational force, the print bead will instead constrict to return to its surface-area-minimizing shape, a phenomena hereafter called “shrink”. With reference to the small overhang in Figure 2.4, Figure 2.5 illustrates the phenomena of sag and shrink.

Sag and shrink are manifestations of the non-ideality of FFF and are undesirable because of their effects on the build process. As a result of sag, the true perimeter surface height lags behind the desired value. As a result

of shrink, the horizontal progression of the structure is stunted. Since FFF printers are open-loop (*i.e.* no feedback between output and input), the control system does not adjust for the difference between the expected and true perimeter positions of the current build layer. Thus, the print head will blindly follow the instructions set out for it in the original g-code without compensating for sag or shrink.

As a further complication, the effects of sag and shrink are not isolated to a single layer but instead compound as more layers are added to the structure. This is because each completed layer becomes the surface upon which the next is built. In the best case scenario, if the number of layers needed to build the inclined feature is smaller than a critical value, the cumulative effects of sag and shrink will not be significant enough to compromise the build process. However, as the height of the feature increases or the overhang angle becomes more severe, the compound sag or shrink may eventually lead to print failure. In this case, the structure would be deemed non-self-supporting.

In essence, the feature slopes and scales dictate the printability of the candidate component. That is, a component with a 45-degree overhang may be printable at one scale but could fail completely when scaled up, due to an increase in the number of layers comprising the inclined feature. Similarly, a sloping surface with an angle exceeding 45 degrees may be printable at a sufficiently small scale (sufficiently few layers). This observation of scale-dependence, in itself, motivates the development of a non-heuristic theory for determination of the critical overhang print angle.

2.1.3 Process Timescales

In evaluating the print bead position/geometry evolution there are two key processes which must be considered, each with their own characteristic timescale.

These are: material flow (post-extrusion) and cooling of the molten polymer (solidification). The relative timescales of each of these two processes will dictate the final position of the extruded filament. The durations described by $t_{solidification}$ and t_{flow} are determined by the material parameters (*i.e.* density, viscosity, surface tension, heat capacity, conduction coefficient, etc.) and the print settings (*i.e.* layer height, nozzle temperature, bed temperature, fan speed, etc.).

In this work we define $t = 0$ as the instant of extrusion. At this point, the bead will have the prescribed height and width, as dictated by the process parameters (volume flow rate and nozzle velocity). Time $t = 0^+$ is the instant of deposition, that is, the moment at which the bead comes into contact and conforms to the substrate (print bed or preceding layer). Lastly, $t = 1$ is the instant at which the bead achieves its final position and geometry, either due to reaching dynamic equilibrium or due to solidification.

2.2 Failure Modes

In order to determine the printability of a candidate component via FFF it's first necessary to classify what constitutes a print success and a print failure. In the context of sag and shrink there are two distinct failure modes. Each of these modes concerns the progression of the structure being built and the compound effects of the aforementioned phenomena. Prior to elaborating on the specifics of the failure modes, we first provide some insight into the relative importance of each of sag and shrink.

2.2.1 Prevalence of Sag and Shrink

The determining factor in which of sag or shrink takes precedence is the relative magnitude of surface tension and gravitational forces, which is summa-

ized by the Bond/Eötvös number. This dimensionless parameter expresses the ratio of gravitational forces to surface forces and is given by the following equation [41].

$$Bo = \frac{\Delta\rho g L^2}{\gamma} \quad (2.1)$$

In (2.1), $\Delta\rho$ is the difference in density between the thermoplastic filament and the surrounding medium (air), g is the constant of gravitational acceleration, γ is the surface tension coefficient, and L is a characteristic length. Here, L is taken to be the radius of a spherical droplet with the same area as the print bead, which we approximate as elliptical for the sake of this calculation but otherwise treat as rectangular for the sake of simplicity. Using the equation for the area of an ellipse with major axis a and minor axis b :

$$A = \pi L^2 = \pi ab, \quad (2.2)$$

$$L = \sqrt{ab} = \sqrt{(w/2)(h/2)}. \quad (2.3)$$

Thus,

$$Bo = \frac{\Delta\rho g wh}{4\gamma}. \quad (2.4)$$

If $Bo > 1$, gravitational forces dominate, whereas if $Bo < 1$, surface tension forces dominate. By extension, if $Bo \gg 1$, sag will be the prevalent phenomena, whereas if $Bo \ll 1$, shrink is the prevalent phenomena. If the Bond number is in the neighborhood of unity (i.e. $Bo \approx 1$), the final bead

position/geometry will be dictated by both surface tension and gravity. That is, the bead will experience both sag and shrink.

For a given material (fixed γ , $\Delta\rho$), Bo will be dictated by h and w , the bead height and width. Thus, the determining factor in how the bead geometry will evolve after deposition is its size, as well as the thermodynamic properties of the process. If the timescale of solidification greatly exceeds that of flow, then the final bead position/geometry will be completely determined by sag/shrink. If the opposite is true, then the bead geometry would be maintained as prescribed. If the timescales are similar, then the equilibrium bead configuration will be somewhere between what is prescribed and what is dictated by gravity and surface tension (sag and shrink).

While sag and shrink are both relevant phenomena in the consideration of material extrusion, as noted, the determining factor in which is prevalent in a particular scenario is the length-scale of the print bead. A survey of the primary applications for fused filament fabrication reveals two disparate length-scales: very small ($\sim 150 \mu m$), as in “desktop” FDM 3-D printers, and significantly bigger ($\sim cm$), as in Large Scale Additive Manufacturing. The disparity between these two length-scales is illustrated in Figure 2.6.

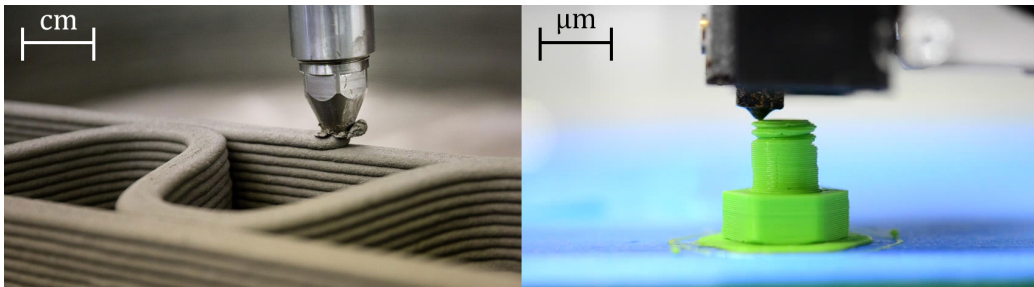


Figure 2.6: Scale comparison of FFF applications. Left: LSAM [42], right: FDM.

The most common application of material extrusion is in desktop FDM 3-D printers, which are used to build components ranging in size from roughly that of a penny to that of a bowling ball. In this scenario, a fine-resolution print would typically have a bead size on the order of the nozzle width ($\sim 400 \mu m$) with a layer height of $\sim 150 \mu m$, while a coarse-resolution print might have a layer height of $\sim 300 \mu m$. The material used for this process is most commonly polylactic acid (PLA) or acrylonitrile butadiene styrene (ABS), with other varieties of thermoplastic also used but less frequently.

Using PLA as a representative material ($\rho = 1240 \text{ kg/m}^3$, $\gamma = 40 \text{ mN/m}$) and considering the difference in layer height for coarse and fine resolution prints, the Bond number ranges from 0.0046 at $150 \mu m$ to 0.0091 at $300 \mu m$. Since, in this case, $Bo \ll 1$, this indicates that when the bead is on the μm scale the gravitational force is negligible in comparison to the surface forces. Thus, the only relevant phenomena in the consideration of the evolution of molten polymer print beads at the scale used in desktop 3-D printers is shrink.

With a bead radius of $r = 1.8 \text{ mm}$, $Bo \approx 1$, while for a bead radius of $r = 1.8 \text{ cm}$, $Bo \approx 100$. Thus, if the bead radius is on the mm scale, sag and shrink will both be relevant, while if it is on the cm scale, sag will dominate. Evaluating these results, we're able to conclude that sag is the primary failure mechanism in large-scale FFF, such as that employed in LSAM or BAAM, while shrink is the primary failure mechanism in small-scale FFF, such as that employed in desktop 3-D printers. This observation essentially allows us to decouple these two phenomena and greatly simplify the analysis of the evolution of print bead geometry in overhanging structures. Due to its increased complexity and limited relevance we choose to omit consideration of intermediate-scale printing, that in which sag and shrink are coupled, and leave that for a future work. Figure 2.7 provides a non-scientific visualization

of the prevalence of sag and shrink as dictated by the Bond number.

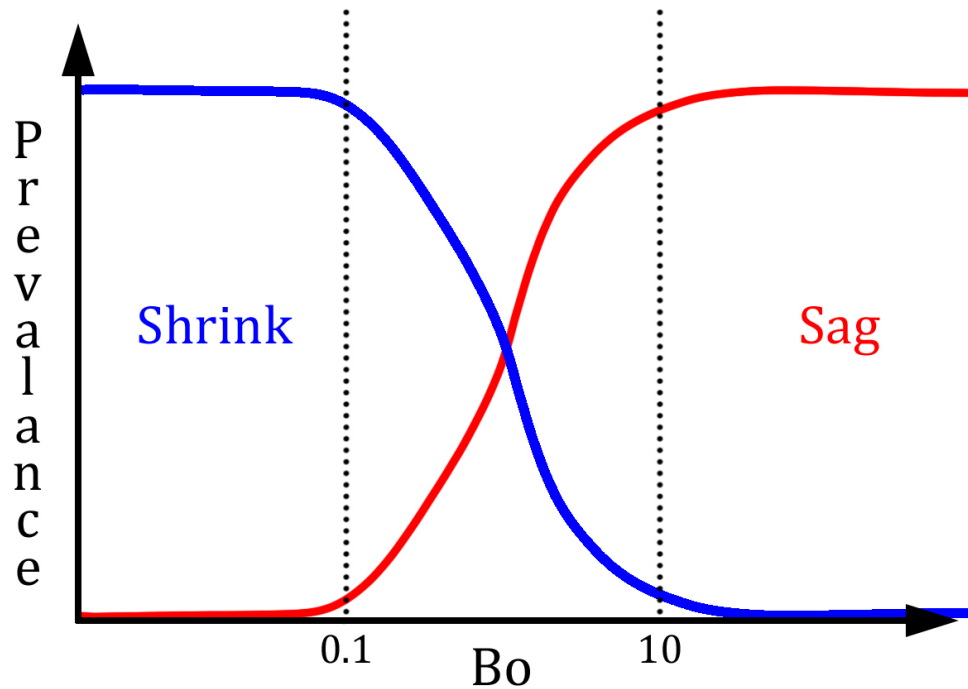


Figure 2.7: Visualization of the prevalence of sag and shrink.

Having now justified the decoupling of sag and shrink, we proceed with defining the failure modes associated with each of these phenomena.

2.2.2 Sag

The influence of sag on the build process is a limiting of the vertical progression of the structure. When sag is present, the unsupported portions of the perimeter extrusions deflect downwards under the influence of gravity. Upon completion, the current layer will become the supporting surface for its successor. Thus, sag in one layer will impact the final position of the bead in the subsequent layer. Without a feedback loop in the control system, the

effects of sag will compound and become magnified with each layer that is added to the structure. Figure 2.8 illustrates the effect of cumulative sag on the print process. The sag, s_i , in layer i , is given by the difference in height (top surface y-coordinate) between the expected and actual equilibrium print bead positions.

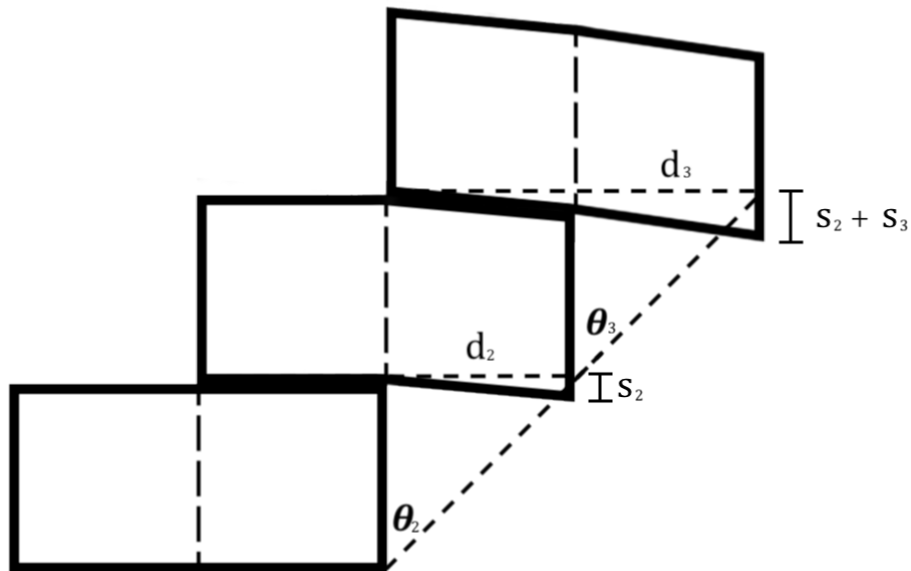


Figure 2.8: Illustration of cumulative sag in stacked layers.

The theoretical sag-induced failure event is defined to occur at the instant in the build process when the cumulative sag exceeds the specified layer height. At this point, the print bead will be one full layer thickness removed from the supporting surface at $t = 0$, meaning that it will only come into contact with the supporting layer once acted upon by gravity. That is, it must fall into place. This may result in the extruded material acquiring momentum before impact, leading to an exacerbated sag effect.

In quantifiable terms, the sag-deduced printability criterion is violated if the following inequality is satisfied, where N is the total number of layers required to print the feature and h is the layer height.

$$\sum_{i=1}^N s_i > h \quad (2.5)$$

2.2.3 Shrink

The second failure mode concerns the other relevant phenomena, shrink. While sag limits the vertical progression of the structure, shrink has an equivalent effect on the horizontal progression. Shrink arises due to the surface tension of the molten polymer. That is, its tendency to want to adopt its surface-energy-minimizing configuration. The bead is initially coerced by the process parameters (volume flow rate, nozzle velocity) and size specifications (nozzle width, layer-layer separation) to attain a specific height and width. Under the influence of inter-layer adhesive forces, and with a large conductive contact area to accelerate solidification, a fully-supported bead will roughly retain this prescribed geometry. On the other hand, in the case of a partially supported bead, as present in an overhanging perimeter strand, the unsupported portion will not benefit from the same adhesive forces or rapid solidification to help maintain its as-deposited geometry.

Shrink describes the change in shape of an overhanging print bead due to surface tension forces. In all practical cases, print parameters are set such that the print bead width is greater than its height, as this increases the contact area between layers and thus the inter-layer adhesion. As such, the net surface tension force is directed such that it tends to cause a horizontal contraction of the bead. Figure 2.9 illustrates the effect of shrink in stacked layers. As in the case of sag, the effects of shrink compound in successive layers.

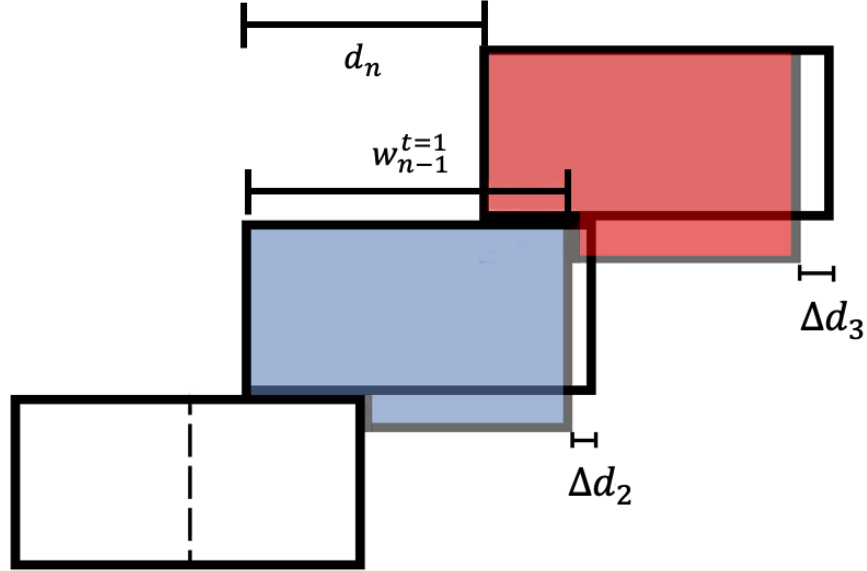


Figure 2.9: Illustration of cumulative shrink in stacked layers.

The shrink-induced failure mode occurs when the overhang offset of the current layer exceeds the equilibrium width of the preceding layer. That is, when:

$$d_n > w_{n-1}^{t=1}. \quad (2.6)$$

At this point, the to-be-deposited bead will be completely offset from the preceding layer, rendering it support-less and resulting in it fully reverting to its surface-tension dictated geometry: cylindrical. The strand will then be completely at the mercy of gravity, with its final resting position dictated by the nozzle trajectory. Without the adhesive force of the supporting layer to facilitate nozzle detachment, the extrusion will be dragged around by the print head until which point as it changes direction,

releasing tension on the strand. At this point, the strand will fall until it is arrested by a portion of the already-built structure or the print bed, an effect hereafter called “droop”.

Figure 2.10 shows the evolution of bead geometry for layers of PLA filament with a prescribed height of $300\ \mu\text{m}$ and width of $450\ \mu\text{m}$ at overhang angles of 45° and 50° . In the case of the 45° overhang, the initial bead geometry (green) shrinks incrementally over the course of the first 7 layers to adopt the geometry outlined in yellow. At this point, the geometry could be said to have reached steady-state as there are no significant differences between the yellow and red outlined beads. Note also that the layers are completely planar (orange lines) and that the steady-state bead geometry is not quite cylindrical, indicating that we have not yet crossed into the droop regime. In the case of the 50° overhang, the bead geometry shrinks from green to yellow and again from yellow to red, with the red outlined bead nearing cylindrical. We also see that the later layers are deflecting downwards, indicating that at this point the print is experiencing droop.

The ability of the print process to proceed in the presence of droop is entirely dependent on the structural geometry, with success being determined by the tolerance for deviation from the original geometrical specifications. If, for instance, a component with rectangular cross-section is supported on three out of four sides, as in figures 2.11 and 2.12, the structure may still be printable in spite of droop. In this case, whether or not the print can be considered “successful” is determined based on the strictness of the tolerances.

Careful examination of figures 2.11 and 2.12 highlights the dependence of droop extent on the overhang angle. The steeper surface slope of the com-

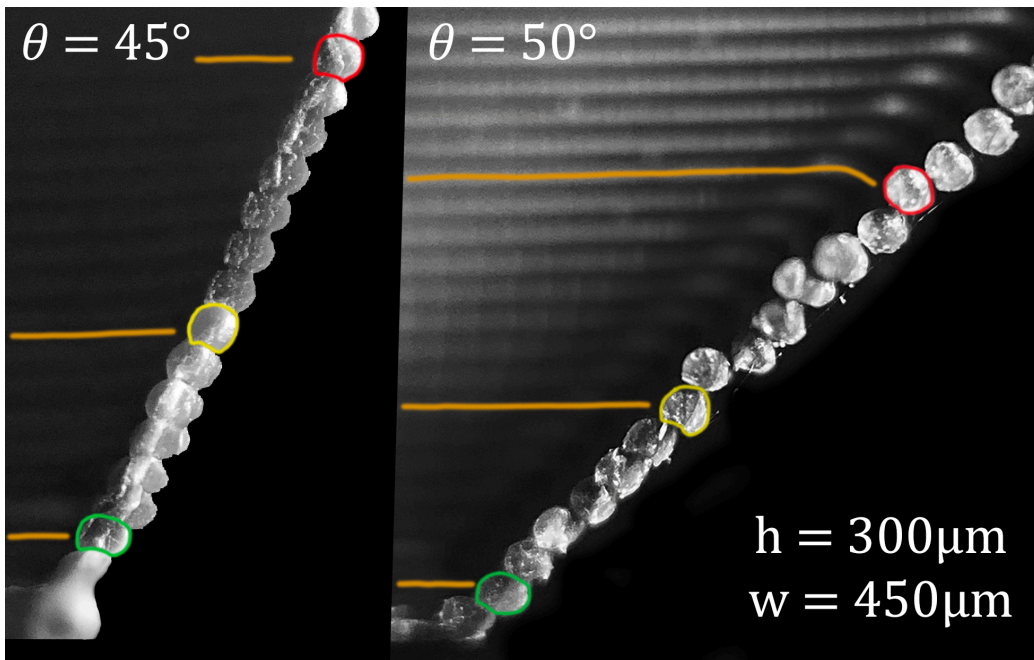


Figure 2.10: Cross-sectional view of overhang feature illustrating evolution of bead geometry due to shrink.

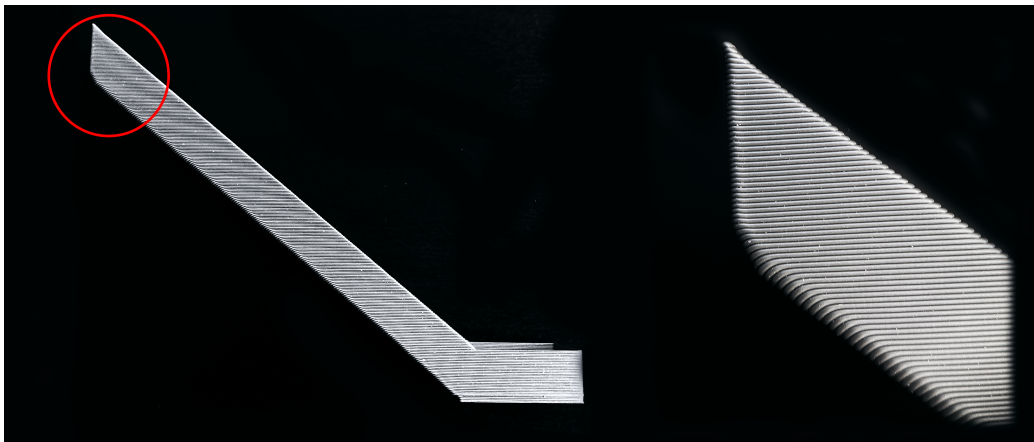


Figure 2.11: Droop illustration for $h = 300\ \mu\text{m}$ and $\theta = 50^\circ$.

ponent in Figure 2.12 results in a much more significant deviation from the intended geometry as compared to Figure 2.11. For reference, the component

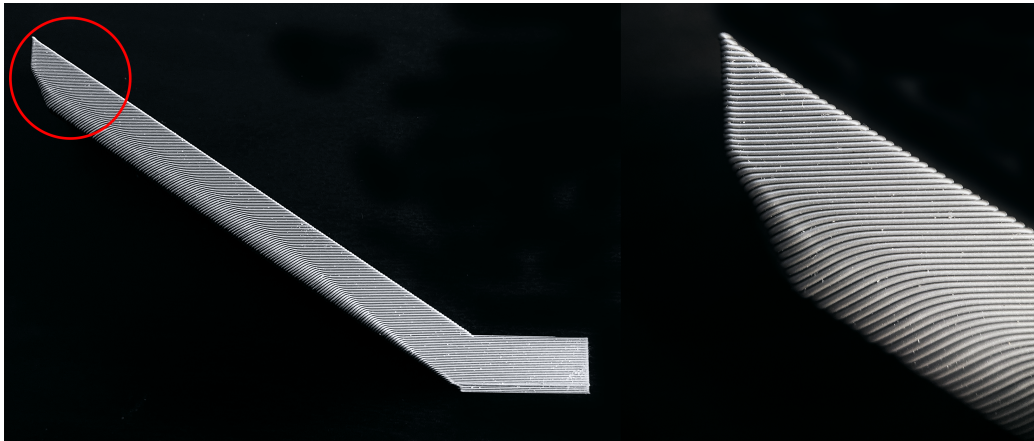


Figure 2.12: Droop illustration for $h = 300 \mu m$ and $\theta = 56^\circ$.

is intended to have a sharp corner where the vertical face meets the bottom inclined surface, but we see here that, in the presence of droop, this is not the outcome. This is illustrated comparatively in Figure 2.13.

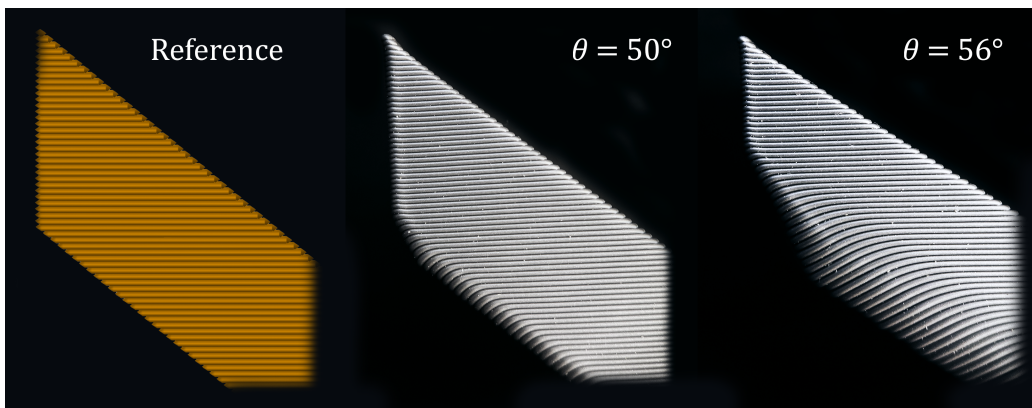


Figure 2.13: Droop reference and comparison.

We next consider an alternate geometry, in which every portion of the perimeter is overhanging, such as the inverted cone. In this case, since no portion of the perimeter is supported, once bead shrink gives way to droop

catastrophic failure soon ensues. This is due to the lack of an adhesive anchor point in the later layers (once in the droop regime), leading to the extrusion not attaching from the nozzle whatsoever.

The reference geometry and print result for an inverted cone with a surface angle of $\theta = 50^\circ$ are given in Figure 2.14. From this figure we can see that the first few layers print successfully, but once the shrink-deduced failure criterion, (2.6), is violated, the print bead no longer detaches from the nozzle. Contrary to the previous example, where only one length of the perimeter was unsupported, the print process cannot proceed once it enters the droop regime. Observing the printer as it is attempting to build this component, we see that the horizontal progression of the structure is stunted by shrink and subsequently by droop, resulting in the nozzle being increasingly displaced from the structure, as indicated in Figure 2.15.

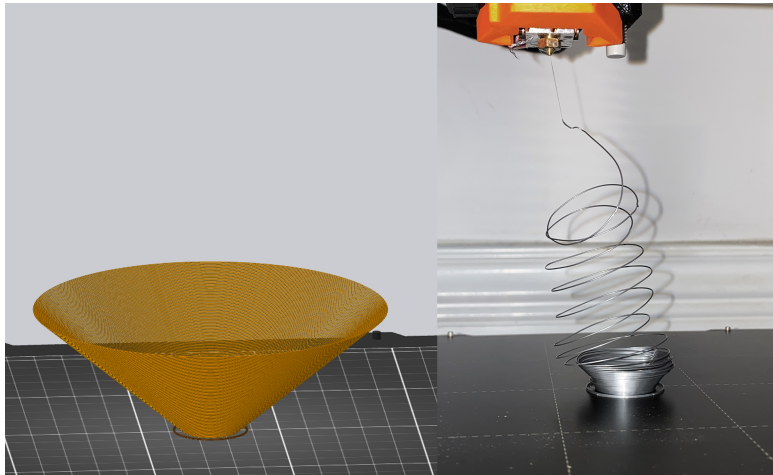


Figure 2.14: Reference geometry and print result for inverted cone with $h = 300 \mu m$ and $\theta = 50^\circ$.

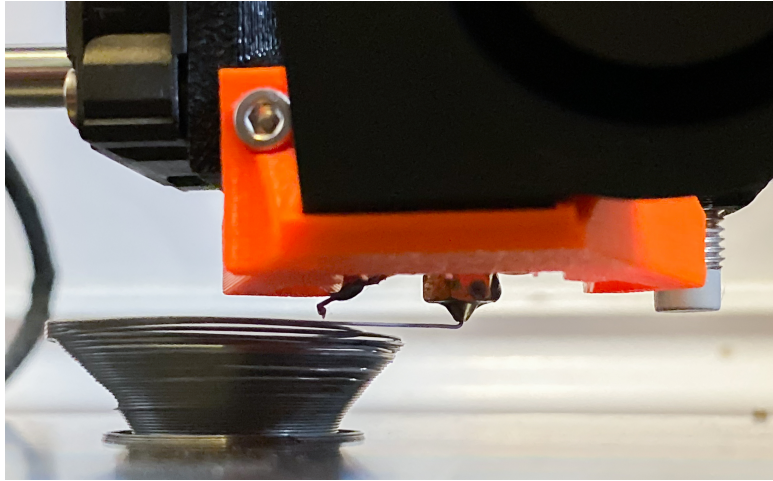


Figure 2.15: Illustration of nozzle-structure offset deviation for inverted cone geometry.

As a final example, we consider a structure that inherits properties of the previous two. The inverted pyramid is similar to the inverted cone in that all of its sides are overhanging. Where it differs, however, is in the nozzle trajectory. In the case of the cone, the circular path means that the direction of the pulling force imparted by the nozzle on the strand is constantly changing. Thus, once in the droop regime the strand will continuously fall away from the nozzle but will not adhere to the previous layer due to the nozzle-structure offset deviation resulting from shrink.

In the case of the inverted pyramid, the nozzle moves in linear segments, periodically turning 90 degrees with respect to its previous direction of travel. At this point, the component of tension also changes direction (for instance, from $-y$ to $+x$), resulting in the previous segment of strand drooping away from the nozzle and coming into contact with the previously deposited layer. This contact then anchors the strand as more material is extruded with the nozzle propagating perpendicularly to its previous direction of travel. Again, when the nozzle reaches the corner point in the geometry its trajectory

changes by 90 degrees, releasing the tension on the strand and allowing it to droop into place, repeating the cycle.

Due to the difference in nozzle trajectory, the pyramidal structure doesn't experience the same degree of nozzle-structure offset deviation as the conic structure, which is illustrated in Figure 2.16. That being said, however, once in the droop regime, the print bead has completely reverted to its surface-tension dictated geometry: cylindrical. Thus, the layer-layer contact is greatly diminished, resulting in very weak inter-layer adhesion which can subsequently lead to delamination, as evidenced by the print result in Figure 2.17. The dependence of contact area on print regime is demonstrated in Figure 2.18, where the red line indicates the extent of contact between stacked layers.

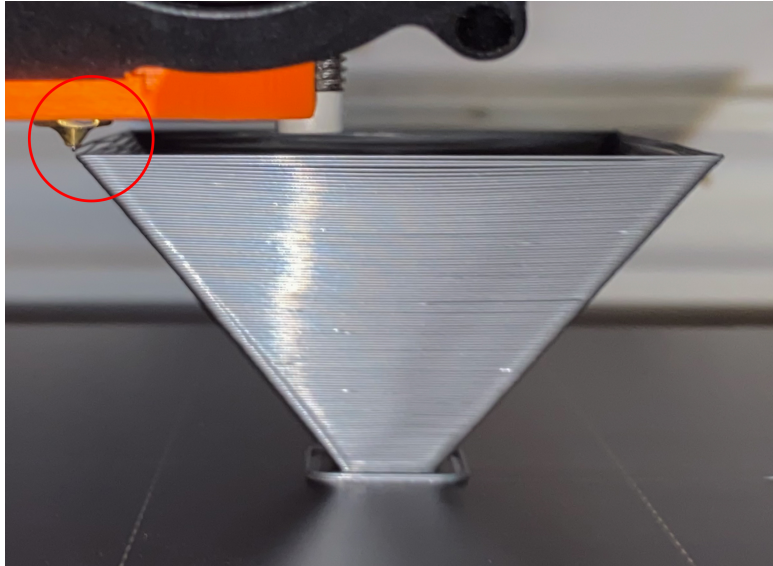


Figure 2.16: Illustration of nozzle-structure offset deviation for inverted pyramid geometry.

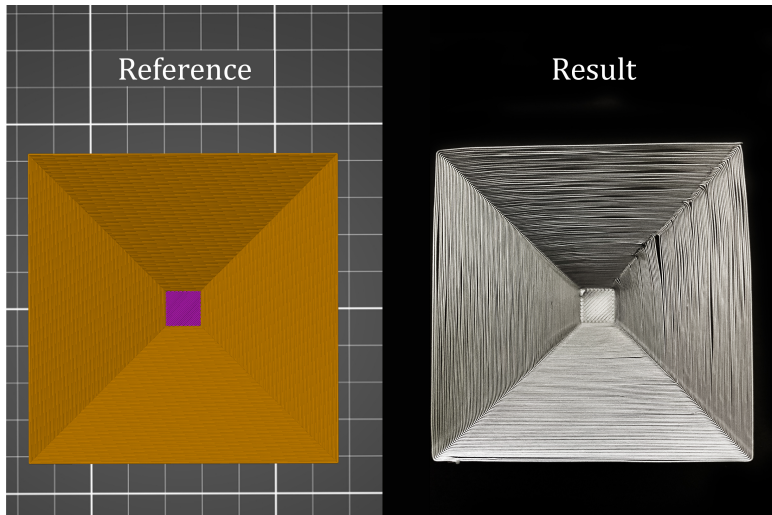


Figure 2.17: Reference geometry and print result for inverted pyramid with $h = 300\mu m$ and $\theta = 56^\circ$.

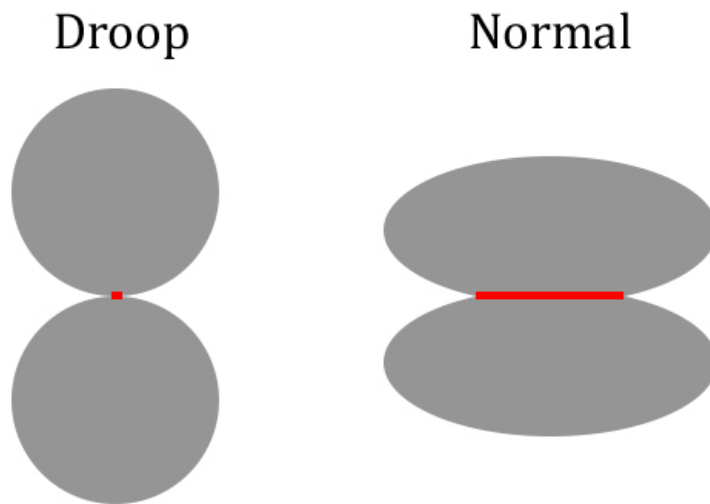


Figure 2.18: Contact area comparison for different print regimes (bead geometries).

2.3 Multiple Perimeters

In FFF a new layer is initiated by the printing of perimeters or “shells”, followed by the printing of infill. The perimeters give the component its structure while the infill adds rigidity and connects any interior and exterior perimeters. Typically, the number of shells is set to two and the infill percentage is varied according to how “solid” the part is desired to be. However, the number of shells can also be varied, in combination with the infill percentage, in order to optimize the component’s strength-to-weight/material consumption ratio. An example of the different infill percentages and number of shells is provided in Figure 2.19. It’s important to note that the shells are generally printed from the inside out (in the direction of increasing perimeter).

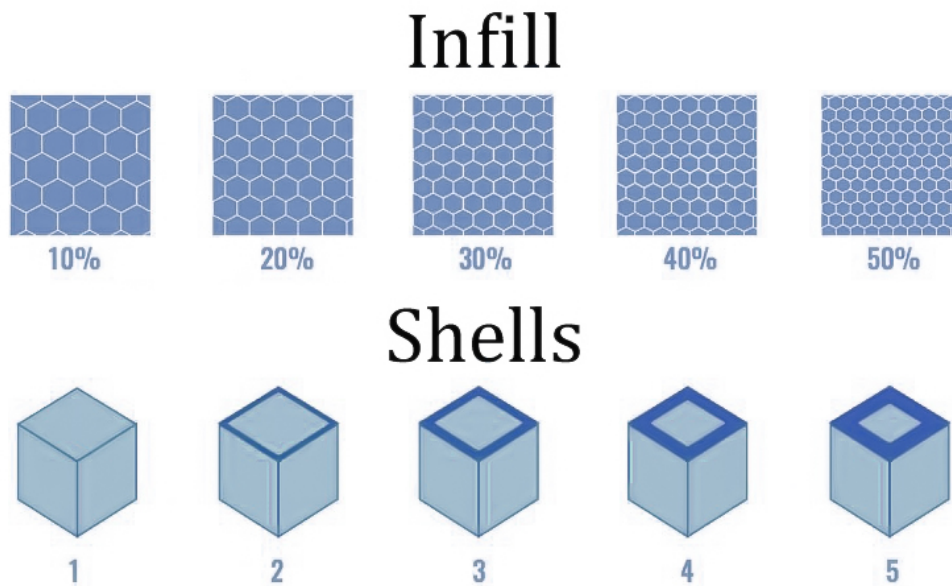


Figure 2.19: Illustration of infill percentage and number of shells. Modified from [43].

While the number of perimeters is typically thought only to affect a component's rigidity, this parameter will also influence the printing of overhangs. Until now sag and shrink have been discussed exclusively in the context of single perimeter overhangs, however, the number of perimeters will, in fact, play an important role in the progression of these phenomena. In the case of sag, the addition of a second perimeter will add an additional conductive contact surface to help the exterior perimeter cool quicker, thus acting to reduce the flow time and therefore the extent of sag. In the case of shrink, the interior perimeter will act to anchor the exterior strand, delaying the onset of droop. At a certain point, depending on the geometry, the bead width of the exterior strand may be reduced by shrink to a sufficient enough extent that the interior strand, which was once fully supported, is now itself overhanging. This will render the interior strand prone to shrink, which may result in the elimination of the adhesive contact between it and the exterior strand, leading to the delayed onset of droop in the exterior strand.

Chapter 3

Model

We now have a theory which allows us to better understand the intricacies of FFF 3-D printing and comprehend why there is a limitation on the angle of surfaces manufactured using this technology. However, we're still lacking a model that can implement this theory to predict the printability of a candidate component based on its geometrical features. In this section we present a first-of-its-kind prediction model for determination of the maximum overhang print angle which takes into account the material characteristics as well as the process parameters.

3.1 Sag – Large-scale FFF

The basis for the sag model is a balance of forces acting on the unsupported portion of the print bead. The relevant forces are gravity and viscous shear. In order to simplify the analysis of the bead dynamics, the geometry is discretized into N rectangles, called “slices”, where N is determined based on the required precision. See figures 3.1 and 3.2 for the slice definition and force diagram.

The objective of the model is to track the position of each material ‘slice’

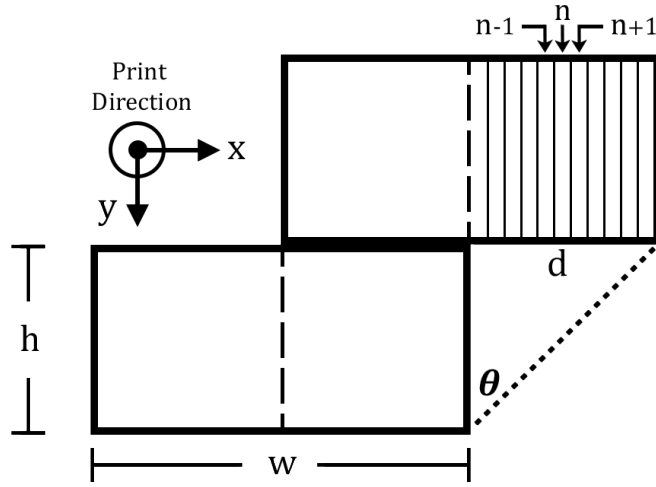


Figure 3.1: Print bead geometry and slice definition.

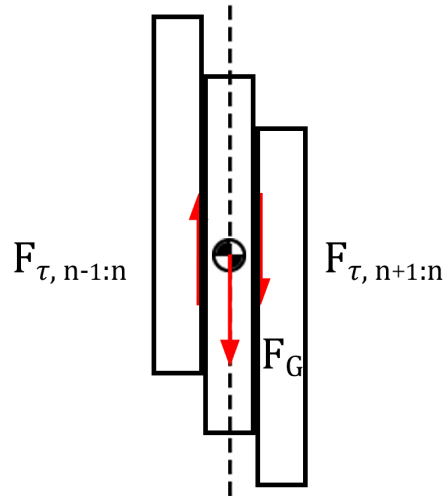


Figure 3.2: Slice force diagram.

over time, terminating when the velocities have been extinguished due to solidification. In this analysis, due to the assumption of high mass/surface tension ratio (*i.e.* high Bond number), we further assume that the unsupported portion of the bead does not impart an appreciable tension force on

the supported portion and vice-versa. Thus, the only interaction between the two portions of the bead is through viscous shear and there is no lateral flow of material.

Due to the influence of the gravitational force, the unsupported slices will initially accelerate. As they do, however, the shear forces, which are velocity-dependent, will act to oppose their motion. In order to determine the extent of sag, it's necessary to know the elapsed time between deposition and solidification. As long as the print bead is still in its liquid or pseudo-liquid form, it will flow under the influence of gravity. Thus, the flow time is equal to the duration for which the polymer melt is above its glass transition temperature ($T_{solidus}$).

3.1.1 Solidification

In order to evaluate the evolving print bead geometry we require a means of tracking the viscosity of the material, which, in the case of a polymer, is temperature-dependent. No real phase change is occurring as the polymer cools, as in the liquid to solid transition of water to ice, but instead the material is simply becoming more viscous (resistant to flow). At a certain point, the viscosity will be so high that for all intents and purposes the material can be considered a solid.

In this analysis the dominant mode of heat transfer is assumed to be bead-strand conduction (*i.e.* the flow of heat from the newly deposited bead to the previously solidified strand in the preceding layer). For the time being we focus on a single perimeter overhang, though consideration of multiple perimeters would only require a slight modification to the heat transfer model. Further, it is assumed that the supported portion of the bead solidifies first, followed by the unsupported portion. This allows us to split the

2-D conduction problem into two separate one-dimensional problems. The temperature as a function of position and time is then given by (3.1), which is the exact solution to a 1-D transient impulse conduction problem [44].

$$\bar{T}(\bar{x}, \bar{t}) = 2 \sum_{n=1}^{\infty} \frac{(-1)^{n-1} \cos(\lambda_n \bar{x}) \exp(-\lambda_n^2 \bar{t})}{\lambda_n} \quad (3.1)$$

$$\lambda_n = \frac{1}{2}(2n - 1)\pi, \quad n = 1, 2, \dots \quad (3.2)$$

$$\bar{x} = \frac{x}{H}, \quad \bar{T} = \frac{T - T_{bed}}{T_{bead} - T_{bed}}, \quad \bar{t} = \frac{t\alpha}{H^2} \quad (3.3)$$

$$\alpha = \frac{k}{\rho c_p} \quad (3.4)$$

An order of magnitude time estimate for the cooling/solidification process is given by the ratio of the change in stored thermal energy to the rate of heat transfer:

$$t_{solidification} = \frac{Q_{supported}}{\dot{Q}_{supported}} + \frac{Q_{unsupported}}{\dot{Q}_{unsupported}}, \quad (3.5)$$

where

$$Q = mCp\Delta T = \rho L H l C p (T_{solidus} - T_{bead}) \quad (3.6)$$

and

$$\dot{Q} = kA \frac{\Delta T}{\Delta y} = kLl \frac{(T_{bed} - T_{bead})}{H} \quad (3.7)$$

from Fourier’s law of heat conduction. In the preceding equations, L is the length of the conductive contact surface between the new bead and the supporting strand, while H is the thickness across which heat is transferred. For the supported portion of the bead, $L = w - d$ and $H = h$, while for the unsupported portion of the bead, $L = h$ and $H = d$. Lastly, l is the extrusion length measured in the print direction. Therefore,

$$t_{solidification} = t_{supported} + t_{unsupported} \quad (3.8)$$

$$= \frac{\rho Cp}{k} [h^2 + d^2] \left(\frac{T_{solidus} - T_{bead}}{T_{bed} - T_{bead}} \right). \quad (3.9)$$

The temperatures present in the above equations are system and material dependent. Representative values are $T_{bed} = 333K$ ($60^\circ C$) and $T_{bead} = 488K$ ($215^\circ C$), which are commonly used when printing with PLA filament. $T_{solidus}$ is the glass transition temperature, the point at which the melt transitions from the “rubbery” state (soft and flexible) to the “glassy” state (hard and brittle). For PLA, $T_{solidus} = 337K$.

It’s worth noting here that while this characterization of heat transfer is relatively simplistic, it is easy to conceive how one might increase the complexity of the model by adding considerations for such things as forced convection or 2-D transient conduction. For the sake of this thesis, however, these were deemed to be outside the scope of work.

Now that we’re equipped with a means of tracking the temperature as it varies in space and time, this can be used to determine the transient spatial viscosity of the bead. Polymers are an example of a shear-thinning non-Newtonian fluid, thus, in addition to being temperature-dependent, the

bead viscosity will also be shear-rate-dependent. We therefore employ the Cross-WLF viscosity model for non-Newtonian fluids, which is described by the following set of equations [45].

$$\mu_0(T) = D_1 \exp \left[\frac{-A_1(T - T^*)}{A_2 + (T - T^*)} \right] \quad (3.10)$$

$$\mu(T) = \frac{\mu_0(T)}{1 + \left(\frac{\mu_0 \dot{\gamma}}{\tau^*} \right)^{1-n}} \quad (3.11)$$

$$T^* = D_2 + D_3 p \quad (3.12)$$

In (3.10) - (3.12), $\mu_0(T)$ is the zero-shear viscosity, μ is the effective viscosity, A_1 , A_2 , D_1 , D_2 and D_3 are material-dependent constants, $\dot{\gamma}$ is the shear rate, n is the power law index, T^* is the glass transition temperature, and τ^* is the critical stress at the transition to shear thinning, determined by curve fitting. The exact values of these parameters can be extracted from material testing data sheets such as those provided by Moldflow [46].

3.1.2 Print Bead Dynamics

Armed with knowledge of the viscosity in each slice, we can then evaluate the shear forces acting within the fluid. To start, we evaluate the velocity at the mid-plane of each slice and the viscosities at the interfaces between slices. As noted, polymer melts are inherently non-Newtonian, meaning that the relationship between shear stress and shear rate is non-linear. However, by employing a marching algorithm for parameter updates and keeping the time step of the viscosity update sufficiently small, we can make a piece-wise constant approximation to the viscosity, and thus, a piece-wise linear approximation to the shear stress/rate relationship. We can then apply Newton's

law of viscosity to determine the inter-slice shear stress for each time step:

$$\tau = \mu \frac{dv}{dx}. \quad (3.13)$$

Considering a representative layer, ‘ n ’, the shear stresses imparted on it by the adjacent layers, $n - 1$ and $n + 1$, are given by the following equations.

$$\tau_{n+1:n} = \mu_{n,n+1} \left(\frac{v_{n+1} - v_n}{\Delta x} \right) \quad (3.14)$$

$$\tau_{n-1:n} = \mu_{n-1,n} \left(\frac{v_{n-1} - v_n}{\Delta x} \right) \quad (3.15)$$

In (3.14) and (3.15) $\mu_{n,n+1}$ and $\mu_{n-1,n}$ are the viscosities at the interfaces between slices $n/n + 1$ and $n - 1/n$, respectively, while v_n is the velocity of slice n and Δx is the slice width and is equal to d/N . Recognizing that the forces are equal and opposite, as dictated by Newton’s 3rd law:

$$\tau_{n-1:n} \Big|_{n=i+1} = -\tau_{n+1:n} \Big|_{n=i}, \forall i. \quad (3.16)$$

Before we can put everything together, we must apply the appropriate boundary conditions for the problem, which are as follows.

$$F_{\tau, n+1:n} \Big|_{n=N} = 0 \quad (3.17)$$

$$a_n, v_n \Big|_{n=1} = 0 \quad (3.18)$$

Equation (3.17) is the free surface condition and (3.18) is the no-slip condition at the interface between the supported (solidified) and unsupported (molten) portion of the print bead.

Finally, completing the force balance on slice n :

$$\Sigma F_{Y_n} = F_g + F_{\tau, n+1:n} + F_{\tau, n-1:n} \quad (3.19)$$

$$\Sigma F_{Y_n} = mg + (\tau_{n+1:n} + \tau_{n-1:n})A = ma_n \quad (3.20)$$

$$m = \rho V = \rho hl \Delta x \quad (3.21)$$

$$A = hl \quad (3.22)$$

$$a_n = g + \frac{(\tau_{n+1:n} + \tau_{n-1:n})}{\rho \Delta x} \quad (3.23)$$

$$= g + \frac{\mu_{n,n+1}(v_{n+1} - v_n) + \mu_{n-1,n}(v_{n-1} - v_n)}{\rho(\Delta x)^2} \quad (3.24)$$

Equation (3.24) gives us the acceleration of slice n at time t due to the influence of gravity and inter-slice shear forces. We are then left with solving a kinematics problem. If we know the initial velocity of the fluid, due to nozzle ejection, we can solve for the velocity of each slice at each instant in time. Using this information, we can then evaluate the y-coordinate of the

slice after each time step. In this formulation, the velocity and acceleration are taken to be constant over the duration of the time step. The parameter update expressions are provided as equations (3.25) and (3.26) below.

Velocity Update:

$$v_{n,t+1} = v_{n,t} + a_{n,t}\Delta t \quad (3.25)$$

Y-Coordinate Update:

$$y_{n,t+1} = y_{n,t} + v_{n,t}\Delta t + a_{n,t}(\Delta t)^2 \quad (3.26)$$

The variable update should be repeated until the velocities are fully extinguished or the interface viscosities have all reached a predetermined threshold. The initial velocity is that of nozzle ejection and is given by the volume flow rate divided by the nozzle area:

$$v_{n,0} = \frac{hwv_{nozzle}}{\pi r_{nozzle}^2}. \quad (3.27)$$

The sag, s_n , for a particular slice, which is what is ultimately desired from the model, is simply the sum of the changes in y-coordinate over each time step. In other words, the total sag for slice n is equivalent to the final y-coordinate of the slice (assuming that $y = 0$ coincides with the common initial centroid position of the slices).

$$s_n = \sum_t \Delta y_{n,t} = \sum_t [v_{n,t}\Delta t + a_{n,t}(\Delta t)^2] = y_{n,t} \Big|_{t=1} \quad (3.28)$$

3.1.3 Implementation

Given the discrete nature of this model, requiring iteration to solve, it is most logical to evaluate it programmatically. The following steps outline the procedure for implementing the model to solve for print bead sag.

Sag Calculation Pseudo-Code

1. Initialize velocities ($v_{n,0}$), temperatures ($T_{n,0}$) and slice positions ($y_{n,0}$)
2. Use temperatures to compute viscosities: $\mu_{n,t}, \forall n$
3. Compute acceleration of each slice from force balance: $a_{n,t}, \forall n$
4. Update slice velocities and y-coordinates: $v_{n,t}, y_{n,t}, \forall n$
5. Increment time step: $t = t + \Delta t$
6. Update T_n and μ_n
7. Repeat steps 2-6 until velocities are extinguished or viscosity threshold is reached

3.1.4 Integration

The output of the sag model is the $t = 1$ positions of the overhanging slices. During execution, the program indicates the current slice positions as well as the slice viscosities, represented by a greyscale colour map. Figure 3.3 shows an example of the slice position evolution. In this figure, the darker the slice, the higher the viscosity. Any slices that are pure black have reached the viscosity threshold and can be considered solidified.

Having obtained the $t = 1$ slice positions in layer l via the sag model, we can then use this information to predict the $t = 0^+$ slice positions for layer

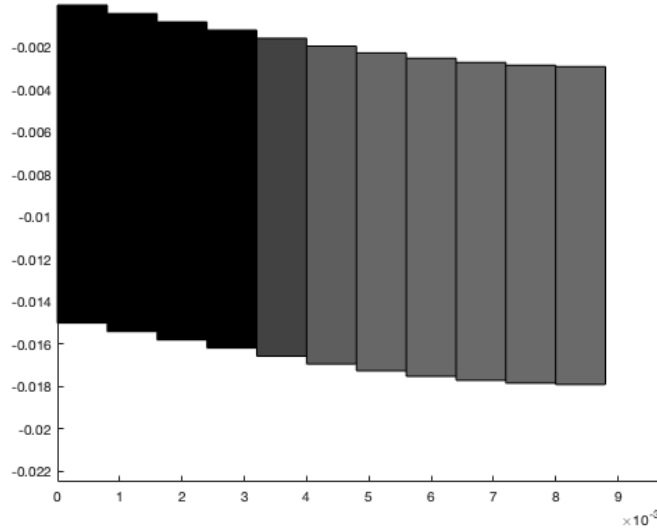


Figure 3.3: Sag model progress example.

$l + 1$. For this purpose, we simply assume that the newly-deposited beads initially conform to the substrate onto which they are deposited. For layer 0 the substrate is the print bed. For every subsequent layer the substrate is the preceding layer.

The $t = 0^+$ bead geometry acts as the input to the sag model while the output is the $t = 1$ geometry. The model is applied iteratively for each layer in the structure. As long as the sag threshold is not surpassed, then the structure is deemed printable. The application of the sag model can be summarized by the following procedure.

Sag Model Application Steps

1. Define $t = 0$ bead geometry (layer height and extrusion width)
2. Predict $t = 0^+$ geometry based on substrate-conformance assumption

3. Apply sag model to determine $t = 1$ geometry
4. Repeat steps 2-3 for as many layers as are required to construct the feature

3.1.5 Results

The complete geometry evolution prediction framework was implemented in *MATLAB* using a viscosity threshold of $5000 \text{ Pa} \cdot \text{s}$. The sag model was executed with an input geometry corresponding to a scaled-up version of the $h = 150 \mu\text{m}$, $w = 400 \mu\text{m}$ print bead. That is, the aspect ratio was fixed at 2.7:1 (w:h). A $50x$ scaling yields a bead Bond number of 10, while $100x$ yields: $Bo \cong 100$. The results for the $50x$ scaling are shown in Figure 3.4, while those for $100x$ are shown in Figure 3.5.

In Figure 3.4 and 3.5 the light grey rectangles represent the prescribed print bead geometry and layer evolution. The darker grey translucent rectangles show the true layer evolution accounting for the effects of sag. At the smaller scale in Figure 3.4 the critical overhang angle is roughly 30° . This is evidenced by the upper right-hand plot, in which the print bead in the 20th layer (top-most dark-grey rectangle) is nearly one full layer height removed from its nominal position (top-most light-grey rectangle). Thus, if one more layer were added to this structure the sag-deduced failure criterion would be met and the structure would be deemed unprintable.

At the larger scale in Figure 3.5, the critical angle is significantly smaller at approximately 20° . This makes intuitive sense because the larger beads have more heat to dissipate, meaning that they take longer to cool and thus flow for longer, leading to increased sag.

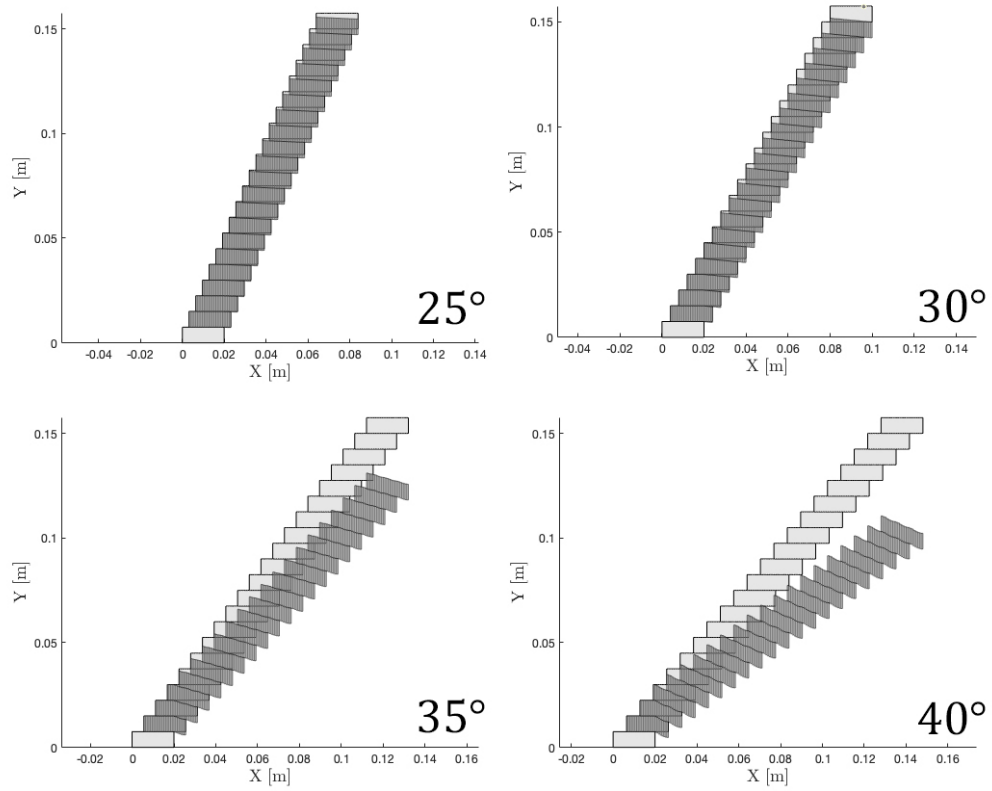


Figure 3.4: Sag model results for a scale factor of 50.

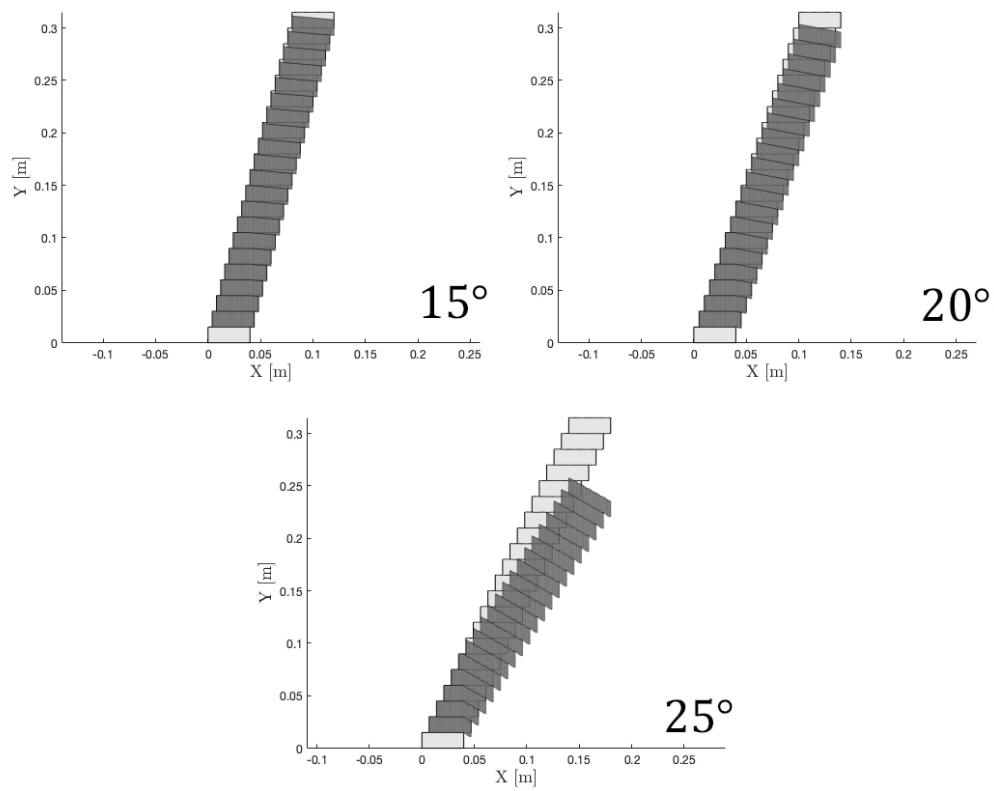


Figure 3.5: Sag model results for a scale factor of 100.

3.2 Shrink – Small-scale FFF

In this section we develop a model that incorporates the theory of print bead shrink in order to predict the printability of a candidate structure via small-scale FFF.

3.2.1 Assumptions

The shrink model centers around the concept of the print bead adopting its minimal surface area configuration, as dictated by surface tension. In it, we assume that because of the high nozzle shear rate at the instant of extrusion ($t = 0$), the shear-thinning polymer initially has a relatively low viscosity, allowing it to achieve its surface-energy-minimizing form at the instant of deposition ($t = 0^+$). Due to the strong inverse correlation between shear rate and viscosity, the viscous forces will quickly increase in magnitude once the nozzle shear has dissipated. Thus, we assume that there is no flow of the bead due to surface tension subsequent to deposition. Further, there will be no gravity-induced flow because of the low mass/surface tension ratio (*i.e.* low Bond number). Therefore, the geometry at $t = 1$ will be equivalent to that at $t = 0^+$.

In order to justify these assumptions, let us consider the viscosity evolution of the print bead during and after nozzle ejection. The pressure-driven progression of the polymer melt through the cylindrical nozzle is a form of Poiseuille flow. In this flow model no slip occurs between the wall and the melt and the velocity is highest at the center. The shear rate can be calculated from the flow rate by way of the following relationship (where the Rabinowitsch correction has been applied to account for the non-parabolic flow at the wall due to the shear-thinning nature of the polymer [47]).

$$\dot{\gamma} = \frac{4Q}{\pi R^3} \left(\frac{3n+1}{4} \right) \quad (3.29)$$

In (3.29), Q is the volume flow rate, R is the nozzle radius, and n is the fluid's power-law index. The most common nozzle diameter in desktop 3-D printers is 0.4 mm and the power-law index for PLA is 0.25 [46]. The flow rate can be calculated as follows.

$$Q = whv_{nozzle} \quad (3.30)$$

A representative value for the nozzle velocity, v_{nozzle} , is 45 mm/s , which is the default value in the printer profile for the *Prusa i3 MK3*. Thus, for a $150 \text{ }\mu\text{m}$ layer height and a bead width equal to the nozzle diameter ($400 \text{ }\mu\text{m}$), the shear rate at the nozzle exit is 188 s^{-1} . Figure 3.6 shows the relationship between shear rate and viscosity of the polymer melt. With a nozzle shear rate of 188 s^{-1} and temperature of 488K , the viscosity upon extrusion ($t = 0$) is $639.73 \text{ Pa}\cdot\text{s}$, which quickly increases to $2918.40 \text{ Pa}\cdot\text{s}$ as the shear rate drops to zero.

3.2.2 Derivation

Under the outlined assumptions, we can proceed to determine the equilibrium bead geometry in a given layer based on the extent of the overhang. The unsupported portion of the bead has an area equal to the total area less the supported area. Thus:

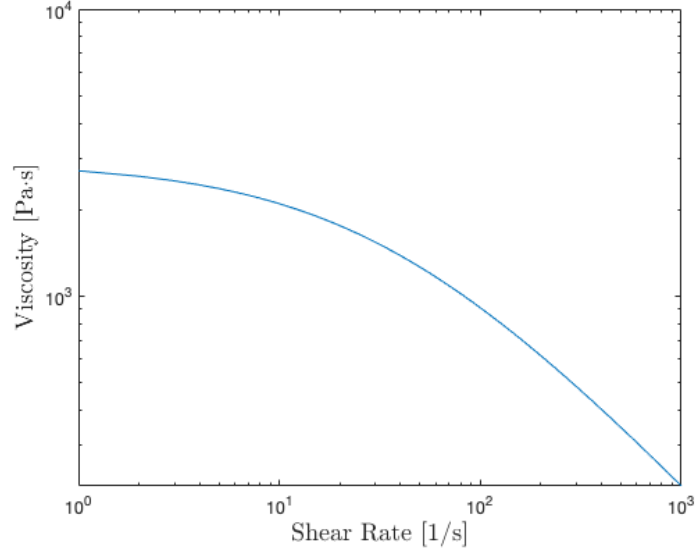


Figure 3.6: Viscosity versus shear rate for PLA.

$$A_{\text{unsupported}} = A_{\text{total}} - A_{\text{supported}} \quad (3.31)$$

$$A_{\text{unsupported}} = hw - h(w - d) = hd = h^2 \tan \theta. \quad (3.32)$$

The surface area of the strand is given by the bead perimeter multiplied by the extrusion length. Thus, the minimal surface area strand is that for which the bead has the smallest perimeter. Given a deformable rectangle with side lengths a , b and area A , the perimeter-minimizing geometry can be derived as follows.

$$A = ab \implies b = \frac{A}{a} \quad (3.33)$$

$$P = 2a + 2b = 2\left(a + \frac{A}{a}\right) \quad (3.34)$$

$$\frac{dP}{da} = 2\left(1 - \frac{A}{a^2}\right) = 0 \implies \boxed{a = \sqrt{A} = b} \quad (3.35)$$

Thus, based on the result of (3.35), the perimeter-minimizing geometry is a square. Therefore, in its surface-energy-minimizing configuration, the unsupported portion of the bead will have side lengths:

$$a = b \equiv c = \sqrt{h^2 \tan \theta} = h\sqrt{\tan \theta}. \quad (3.36)$$

The print bead geometry evolution is illustrated in Figure 3.7. Note that the larger the overhang angle, the greater the extent of shrink. The reduction in bead width (*i.e.* the shrink) is given by (3.37).

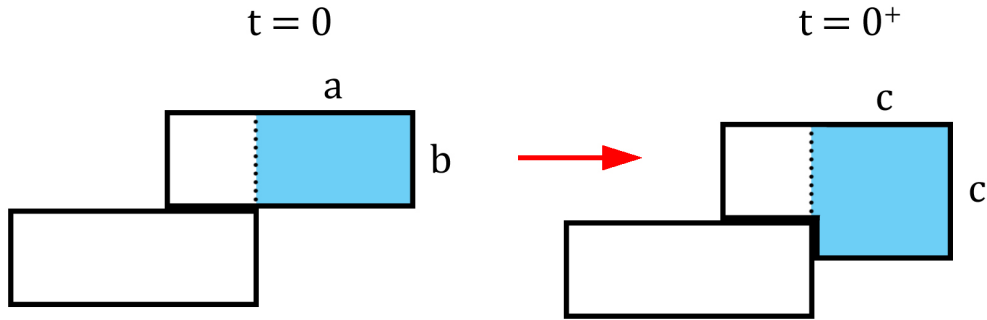


Figure 3.7: Print bead geometry evolution due to shrink.

$$\Delta w \equiv \mathcal{S} = d - c = h \tan \theta - h\sqrt{\tan \theta} = h(\tan \theta - \sqrt{\tan \theta}) \quad (3.37)$$

With knowledge of the bead aspect ratio, $w/h \equiv AR$, the shrink expression can be recast as a percentage reduction in bead width. Thus:

$$\mathcal{S}(\%) = \frac{\Delta w}{w} \cdot 100\% = \frac{1}{AR}(\tan \theta - \sqrt{\tan \theta}) \cdot 100\%. \quad (3.38)$$

As an example, consider a bead with $h = 150 \mu m$ and $w = 400 \mu m$ ($w/h = 8/3$). The shrink percentage as a function of overhang angle for this geometry is illustrated in Figure 3.8.

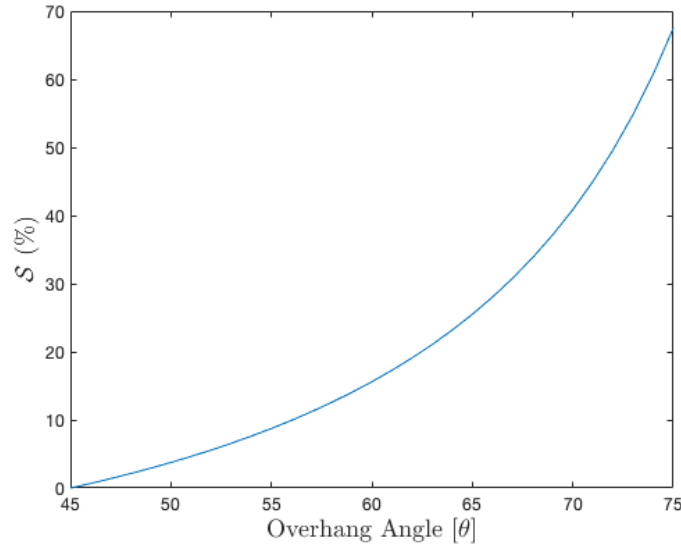


Figure 3.8: Shrink percentage versus overhang angle.

Observe that at $\theta = 45^\circ$, the shrink percentage is zero. This makes intuitive sense because when $\theta = 45^\circ$, $\tan \theta = 1$ and thus, $d = h$. That is, the unsupported portion of the bead is already in its surface-energy-minimizing form and therefore no shrink occurs. For angles less than 45° we assume that there is no appreciable shrink.

The reduction in bead width due to shrink results in an increase in the

unsupported length of the bead in the subsequent layer. For instance, if the overhang angle and layer height combination dictates an offset of d and layer $n - 1$ experiences shrink in the amount of \mathcal{S}_{n-1} , then the unsupported length of layer n will be increased by \mathcal{S}_{n-1} . In general:

$$\mathcal{D}_n = d + \mathcal{S}_{n-1}, \quad (3.39)$$

where $d = h \tan \theta$ is the prescribed horizontal offset and \mathcal{D} expresses the actual offset incorporating the contribution of shrink.

3.2.3 Multiple Perimeters

Consideration of multiple perimeters is achieved through a simple extension of the current model. The interior perimeter is partially supported by its predecessor with the other portion being supported by the exterior strand in the preceding layer. As long as the interior strand is fully supported it will not experience any shrink and thus its geometry will remain unchanged. However, if the overhang is extreme, at a certain point, the width of the strand in the exterior perimeter may have been reduced by shrink to a significant enough extent that the interior strand is no longer fully supported. At this point, it too will be prone to shrink.

Once the width of the bead in the interior strand is reduced by even a small fraction, it will no longer provide an adhesive contact to its neighbouring exterior strand and thus, the exterior strand will begin to experience droop. Effectively, the role of the interior strand is to delay the onset of droop in the exterior strand, thereby increasing the maximum overhang print angle. The failure criterion is as follows:

$$\mathcal{D}_n^{interior} = d_n - w + \mathcal{S}_n > h. \quad (3.40)$$

Failure is defined to occur when the apparent overhang offset of the interior strand, $\mathcal{D}_n^{interior}$, exceeds the layer height, since this corresponds to an equivalent overhang angle of 45° and thus marks the onset of shrink. Note that only the first interior perimeter plays a role in delaying the onset of droop. The addition of any further perimeters beyond two will have no influence on the failure criterion.

3.2.4 Implementation

The shrink model, as described, was implemented in *MATLAB*. The program takes as input the geometrical specifications of the print bead (height and width) as well as a vector of overhang angles that describes the progression of the candidate structure. Based on the layer height and overhang angle, the corresponding horizontal offset for the first layer is calculated. The minimal-surface-area concept is then employed to determine the extent of shrink in that layer. The next layer's $t = 0^+$ geometry is subsequently determined based on the shrink in the previous layer, using (3.39) to evaluate the true overhang offset. This procedure is repeated until the shrink inequality, (2.6), is violated. That is, until the overhang offset in layer n exceeds the width of the bead in the preceding layer ($w_{n-1}^{t=1}$).

Consideration of two perimeters is achieved by adding a variable update/tracking step for the width of the bead in the interior perimeter. The termination condition is also modified to reflect the delayed onset of droop, with (2.6) being replaced by (3.40).

3.2.5 Results

The model was executed with a variety of different combinations of layer heights and overhang angles. Figure 3.9 shows the print bead geometry evolution for a layer height of $150\ \mu m$ and width of $400\ \mu m$, with constant overhang angles ranging from $45^\circ - 60^\circ$. Analyzing these results, we see the effect that shrink has on the width of the bead. At an overhang angle of 60° , the bead width gets progressively smaller until which point as it is exceeded by the horizontal offset. At this point the newly-deposited beads are completely unsupported, marking the onset of droop (not reflected here).

The plots for a layer height of $300\ \mu m$ show similar results, though the effects of shrink are not as pronounced because of the smaller aspect ratio of the prescribed bead geometry. In this case, the onset of droop occurs at an overhang angle of approximately 50° . Comparing these results with those for $h = 150\ \mu m$, we see that the onset of droop occurs a full 10° sooner.

We next consider a structure with $h = 150\ \mu m$ and a non-constant overhang angle which ranges from $20^\circ - 65^\circ$ in increments of $0.5^\circ/\text{layer}$. The bead geometry evolution for this structure is shown in Figure 3.11, alongside a plot of the bead width and overhang offset. This plot indicates that the shrink-deduced failure criterion is met around layer 80. This is when the overhang offset exceeds the bead width, beyond which point the newly deposited beads are completing unsupported, marking the onset of droop.

Multiple Perimeters

If we were to instead print this structure with two perimeters, it would, in fact, be printable. This is evidenced by the results in Figure 3.12. We see here that, while the shrink-deduced failure criterion is met for the exterior

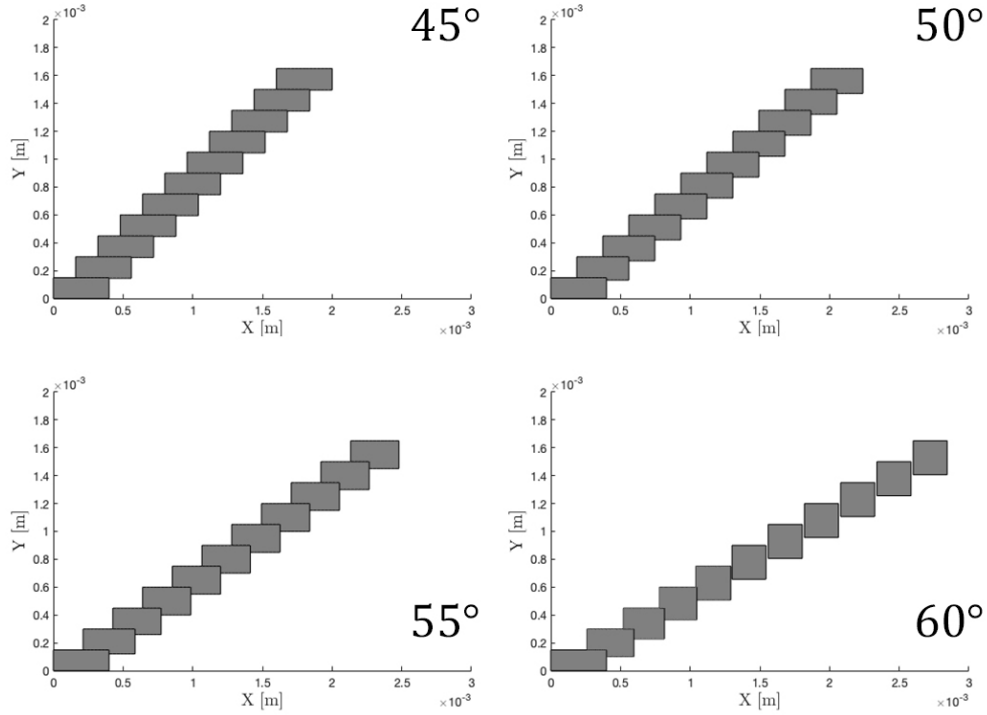


Figure 3.9: Shrink model results for $h = 150 \mu m$

perimeter (red), it is not for the interior perimeter (grey). Thus, the print is able to proceed.

Figures 3.13 - 3.15 show the layer progression with two perimeters for overhang angles of 60° , 69.5° , and 75° . The right-hand plot in each of these figures compares the overhang offset against the bead widths in the two perimeters. As long as the overhang offset doesn't exceed the interior perimeter's bead width, the print will not experience droop. Based on these results, the critical overhang print angle for a layer height of $150 \mu m$ and bead width of $400 \mu m$ with 2 perimeters is roughly 69.5° . Beyond this point, the print will experience droop.

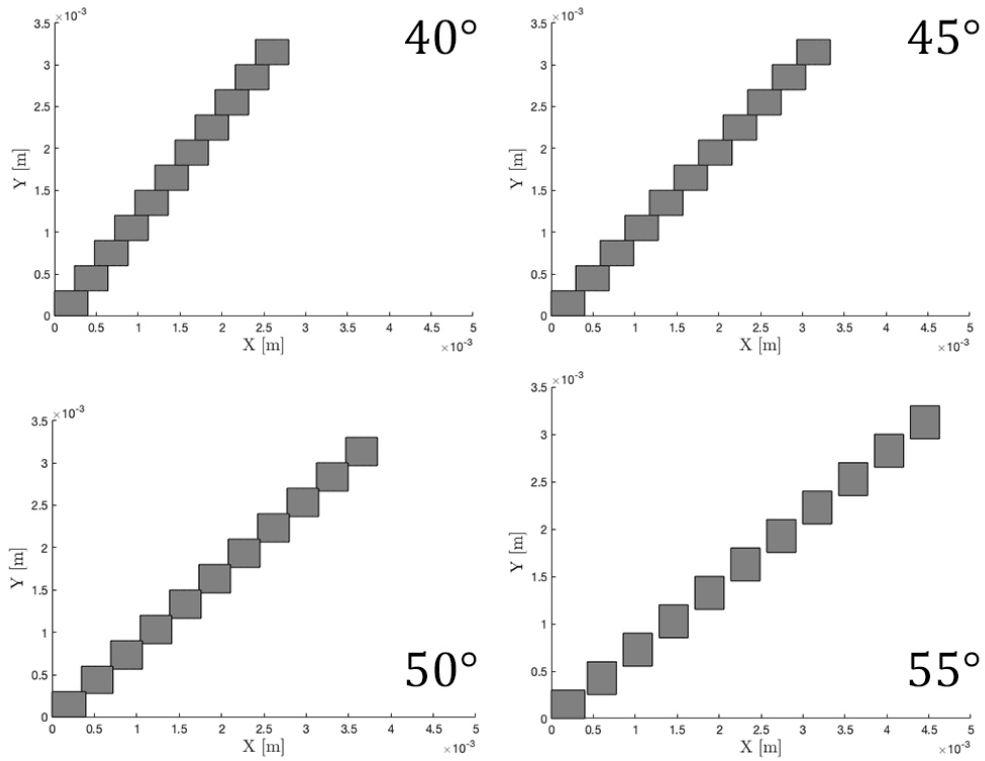


Figure 3.10: Shrink model results for $h = 300 \mu\text{m}$

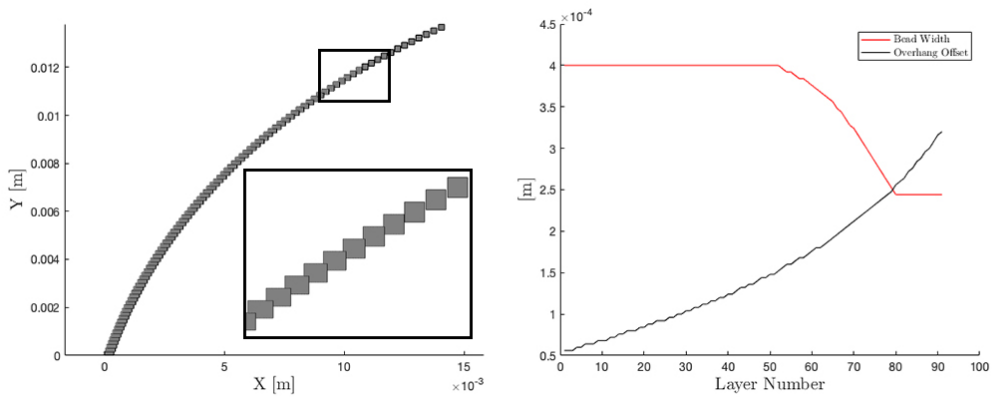


Figure 3.11: Left: layer progression with variable overhang angle; Right: bead width v.s. overhang offset.

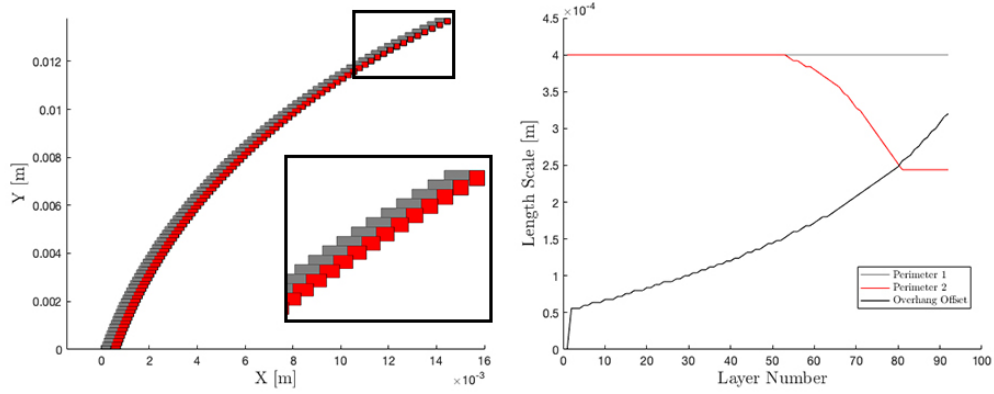


Figure 3.12: Left: layer progression with variable overhang angle and two perimeters; Right: bead width v.s. overhang offset.

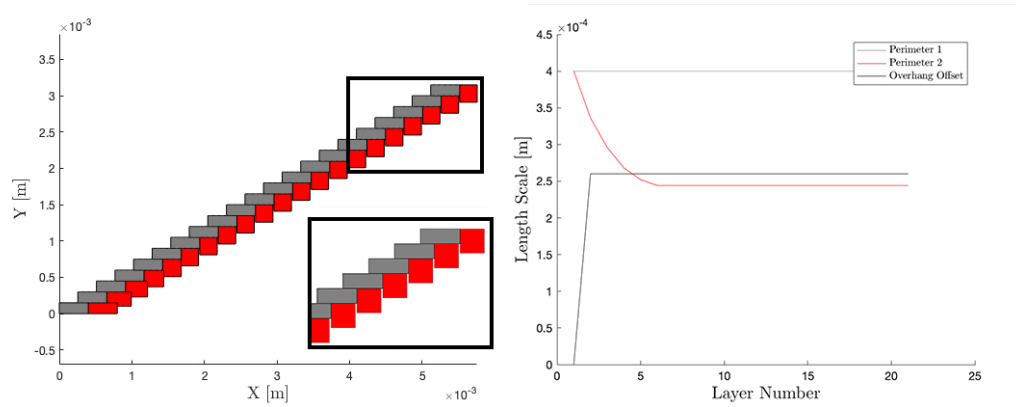


Figure 3.13: Layer progression for $h = 150 \mu m$, $\theta = 60^\circ$ and 2 perimeters.

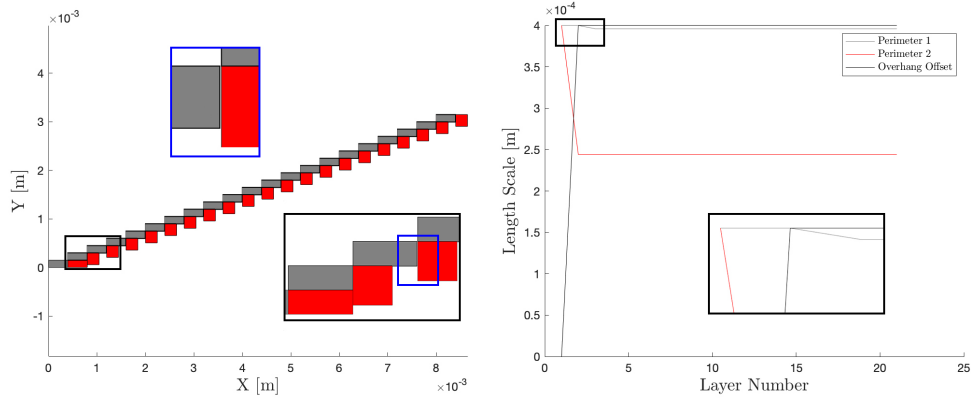


Figure 3.14: Layer progression for $h = 150 \mu m$, $\theta = 69.5^\circ$ and 2 perimeters.

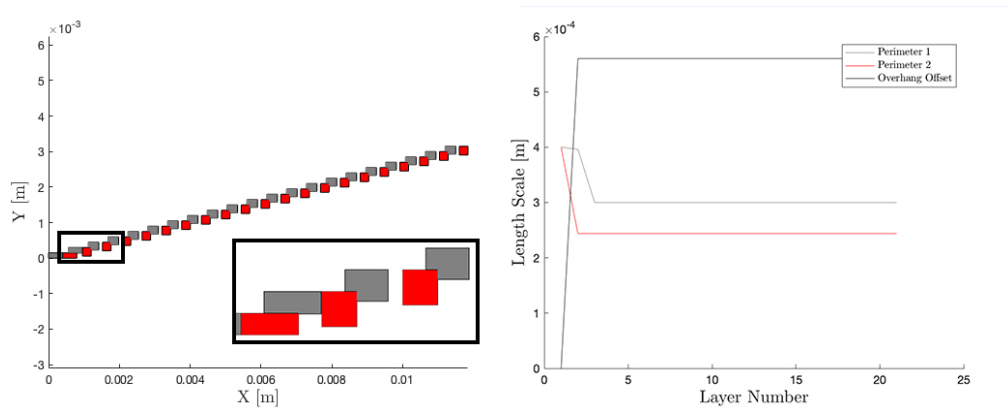


Figure 3.15: Layer progression for $h = 150 \mu m$, $\theta = 75^\circ$ and 2 perimeters.

Chapter 4

Experimental Validation

In order to validate the results of the model a variety of print tests were performed. Unfortunately, we did not have access to a large-scale FFF machine and so the validation efforts were focused on the shrink model. The configuration parameters for the experimental setup are provided in Table 4.1.

Table 4.1: Experimental setup

| | |
|-----------------|--------------------------|
| Printer | Prusa i3 MK3 |
| Slicer | PrusaSlicer |
| Filament | Prusa PLA |
| T_{nozzle} | 215°C |
| T_{bed} | 60°C |
| Print Speed | 45 <i>mm/s</i> |
| Infill | 0% |
| Perimeters | 1/2 |
| Extrusion Width | 0.4 <i>mm</i> |
| Layer Height | 150 μm /300 μm |

The model used for the print tests is illustrated in Figure 4.1, where the incline angle was parameterized.

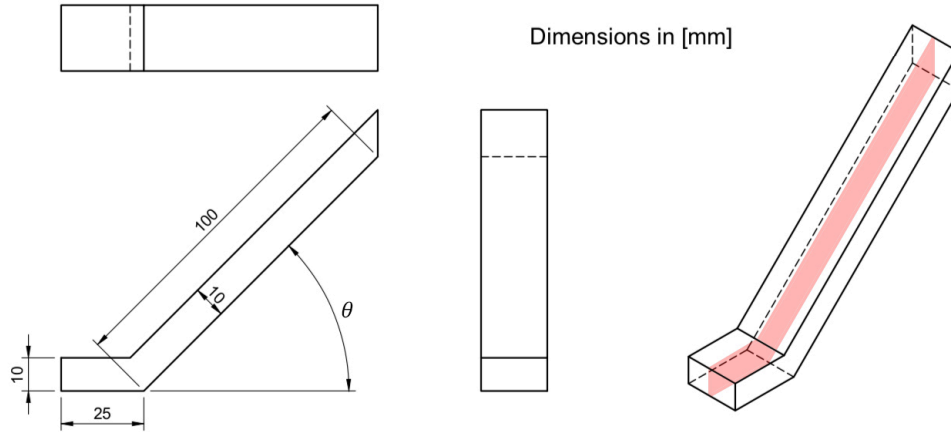


Figure 4.1: Test object geometry.

Tests were conducted with both single and dual perimeters for a range of incline angles. These results were then compared to the model output to assess the accuracy of the predictions.

4.1 Single Perimeter

The results for the single perimeter print tests are illustrated in figures 4.2 – 4.9. The left-hand image in each of these figures shows the model-predicted layer progression based on the shrink theory and generated by the *MATLAB* implementation. The right-hand image shows the true layer progression as observed through a macro lens. These photographs were captured by cutting the printed components in half to achieve a cross-sectional view. The section plane is shown in red in Figure 4.1.

Figures 4.2 – 4.5 show the layer progression for a layer height of $150 \mu m$, while figures 4.6 – 4.9 are for a layer height of $300 \mu m$. In the case of the former, the model predicts the onset of droop between 60° and 65° . Examining the experimental results, we see that the layers are barely in contact at 60° and are completely offset from one another at 65° , which agrees well with the model predictions. Note that the cutting process to achieve the cross-sectional view is somewhat destructive. At more extreme overhang angles, the reduced layer-layer contact results in diminished inter-layer adhesion, and thus the layers are prone to delamination during sectioning. This explains the skewed positioning of the layers in Figure 4.5 and similar.

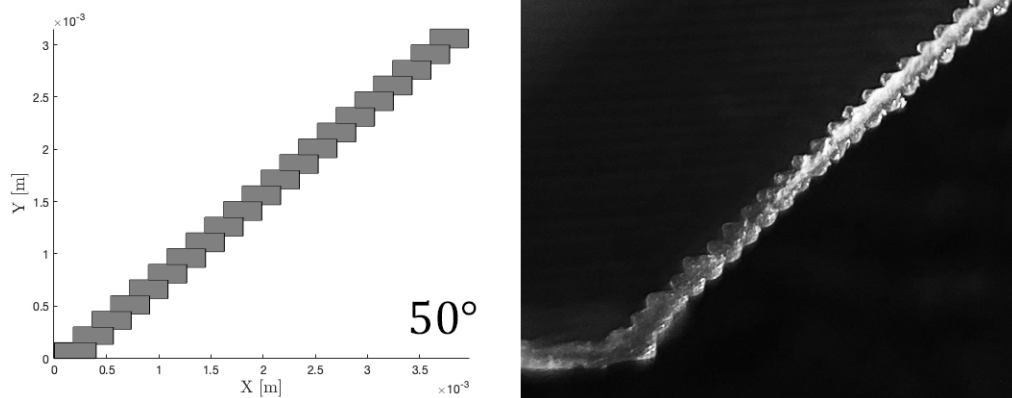


Figure 4.2: Results comparison for $h = 150 \mu m$ and $\theta = 50^\circ$. Left: model, right: experiment.

The model results for a layer height of $300 \mu m$ indicate the onset of droop at 50° . Comparing this to experiment (Figure 4.9), we see that at 50° , the print beads are approximately cylindrical, the layers detach during sectioning and the strands experience droop. Thus, the model predictions are accurately reflected by the experimental findings.

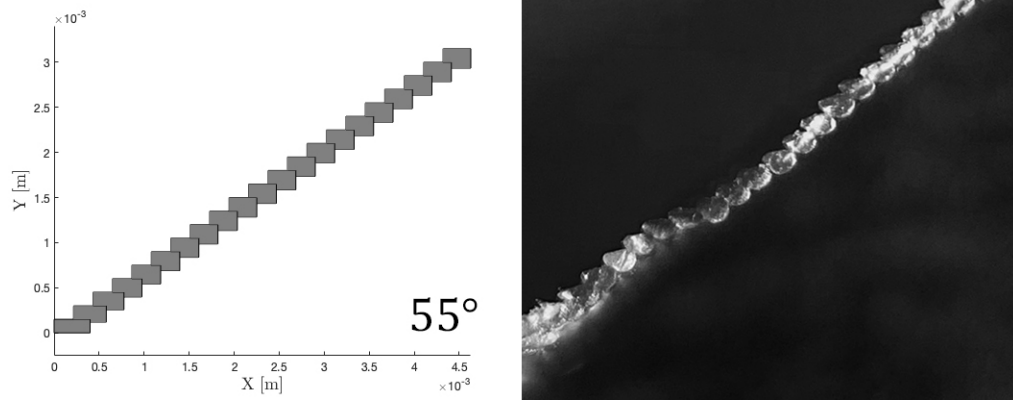


Figure 4.3: Results comparison for $h = 150 \mu m$ and $\theta = 55^\circ$. Left: model, right: experiment.

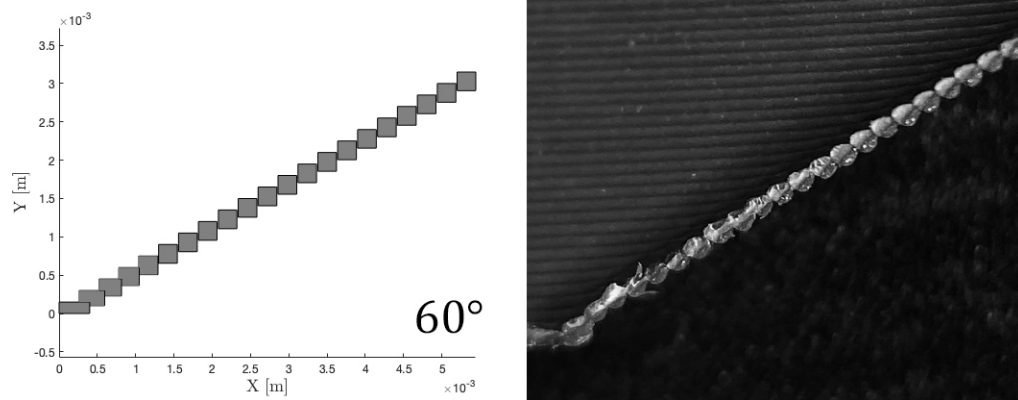


Figure 4.4: Results comparison for $h = 150 \mu m$ and $\theta = 60^\circ$. Left: model, right: experiment.

Contrasting the results for the two different layer heights, we see that the $300 \mu m$ layers experience the onset of droop a full 10° sooner than the $150 \mu m$ layers. This makes intuitive sense because, referring back to Figure 1.5, the overhang offset is proportional to the layer height. Thus, taller layers will necessitate larger overhangs in order to achieve the same surface angle.

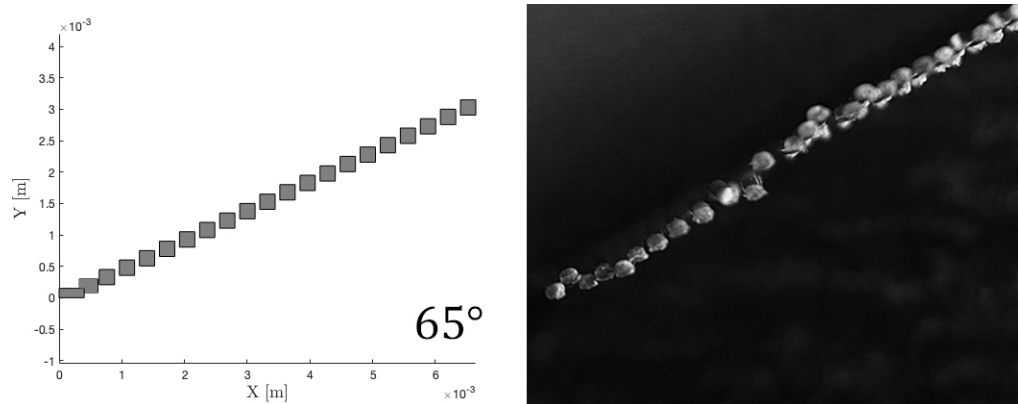


Figure 4.5: Results comparison for $h = 150 \mu m$ and $\theta = 65^\circ$. Left: model, right: experiment.

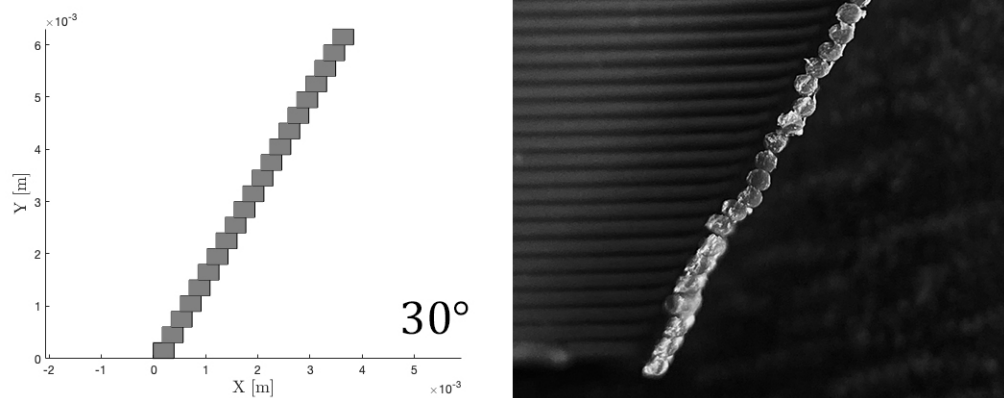


Figure 4.6: Results comparison for $h = 300 \mu m$ and $\theta = 30^\circ$. Left: model, right: experiment.

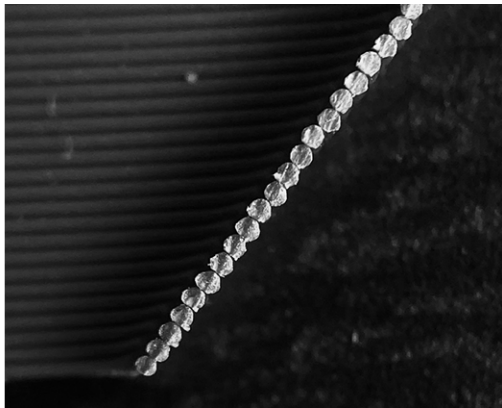
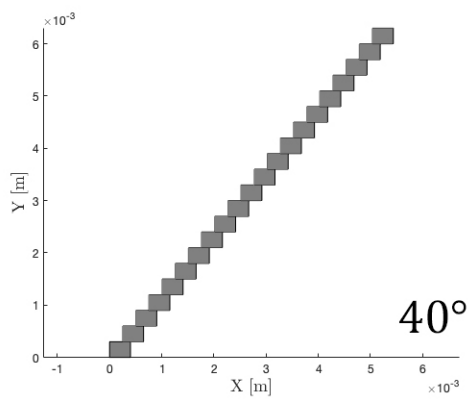


Figure 4.7: Results comparison for $h = 300 \mu m$ and $\theta = 40^\circ$. Left: model, right: experiment.

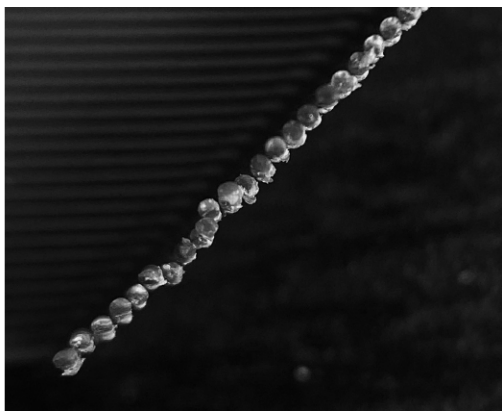
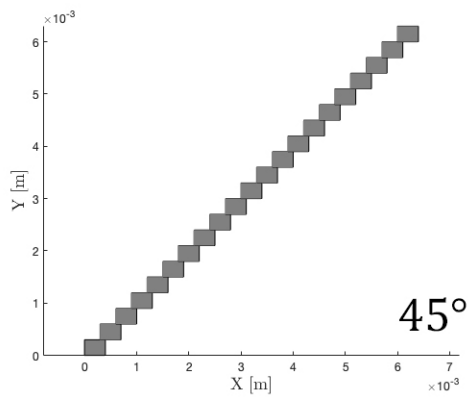


Figure 4.8: Results comparison for $h = 300 \mu m$ and $\theta = 45^\circ$. Left: model, right: experiment.

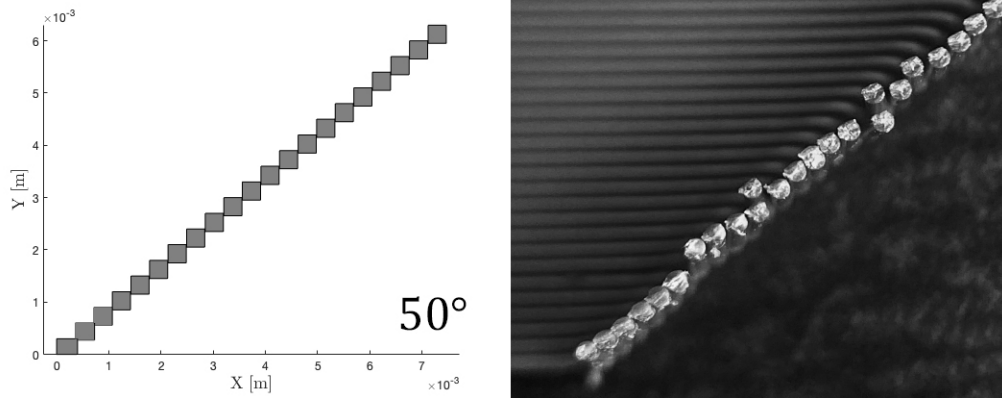


Figure 4.9: Results comparison for $h = 300 \mu m$ and $\theta = 50^\circ$. Left: model; right: experiment.

4.2 Multiple Perimeters

Besides the addition of a second perimeter, the settings for the dual perimeter print test were identical to those for a single perimeter. The results of these tests, which were focused on a $300\ \mu\text{m}$ layer height, are illustrated in figures 4.10 – 4.12. Examining these figures, we see that the addition of a second perimeter has the predicted effect. The internal perimeter acts to anchor the external perimeter, delaying the onset of droop.

With two perimeters, the model predicts the onset of droop at around 68° . This is reflected by the experimental findings, in which, at 68° , the beads in both the internal and external perimeters have reverted to their surface-tension dictated geometry and droop is observed.

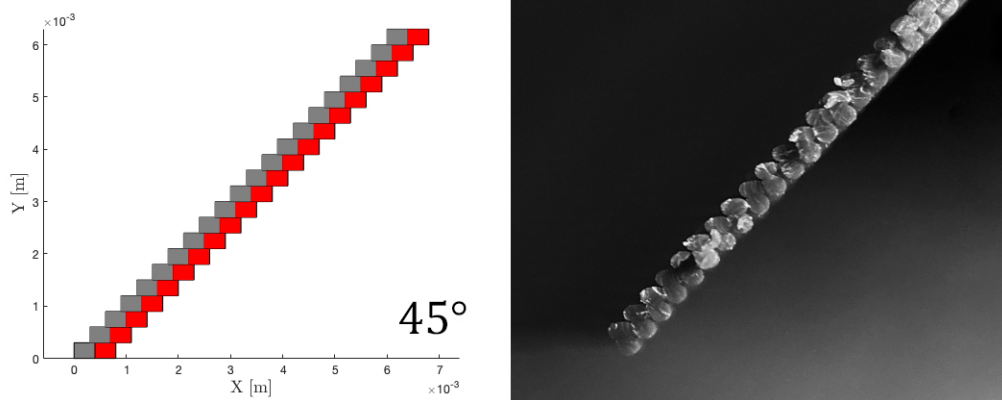


Figure 4.10: Results comparison for $h = 300\ \mu\text{m}$ and $\theta = 45^\circ$ with 2 perimeters. Left: model, right: experiment.

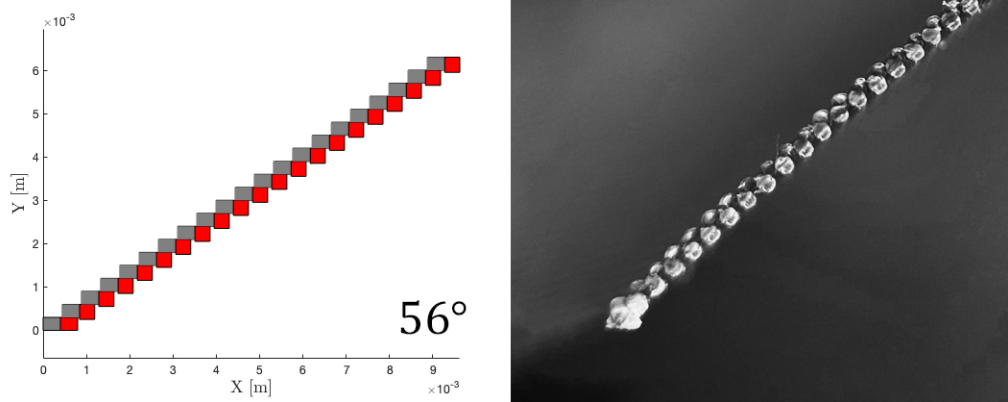


Figure 4.11: Results comparison for $h = 300 \mu m$ and $\theta = 56^\circ$ with 2 perimeters. Left: model, right: experiment.

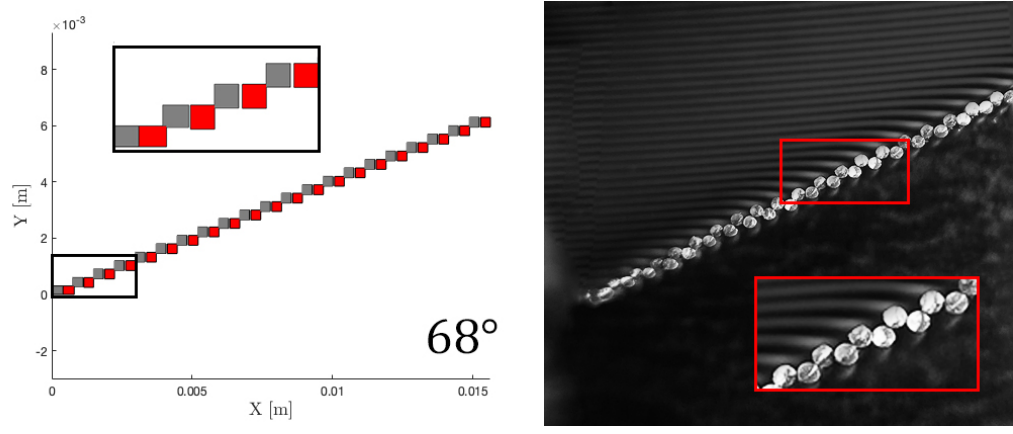


Figure 4.12: Results comparison for $h = 300 \mu m$ and $\theta = 68^\circ$ with 2 perimeters. Left: model, right: experiment.

Chapter 5

Results and Discussion

The purpose of the experimental validation was to assess the appropriateness of the model and the accuracy of its predictions. In the previous chapter we presented the findings for a combination of layer heights, surface angles, and perimeter configurations. The results indicate that the model has good adherence to reality and can accurately predict the onset of droop for both single and dual perimeter configurations with various layer heights.

The evidence indicates that the maximum overhang angle is inversely proportional to the layer height. That is, it is possible to print structures with more extreme surface angles when the layer height is smaller. The maximum overhang angle is also increased with the addition of an interior perimeter as this delays the onset of droop.

In theory, this model could now be used to predict the critical overhang print angle based on the print parameters (extrusion width, layer height and number of perimeters). Of course, as noted earlier, the model simply predicts the onset of droop. How the droop is manifested, and whether or not the print can proceed, depends on the particular geometry.

Lacking access to a large-scale FFF printer, we were unable to validate the results of the sag model. However, the theory, as presented, still has value. The main takeaway is that the maximum overhang angle in large-scale FFF is limited by gravity. This insight can be used to inform any modifications to the process parameters in order to improve overhang print performance. For instance, the maximum overhang angle could theoretically be increased by printing with a less dense material or in a low-gravity environment. These same modifications would not achieve the desired effect in small-scale FFF.

The sag model results indicated that the maximum overhang angle is scale-dependent. This was evidenced by the fact that the maximum angle was lower at the 100x scale than it was at the 50x scale. This is presumed to be a result of the higher heat capacity of the larger bead, requiring longer to solidify and thus allowing more time for flow. Based on these results, we can infer that the maximum overhang angle could be increased by increasing the rate at which heat is removed from the molten print bead. For instance, by adding a cooling fan.

5.1 Conclusions and Future Work

In this work we have presented a first-of-its-kind theory to describe the limiting phenomena in the manufacture of structures with inclined surfaces via fused filament fabrication. Terminology was introduced to describe these phenomena and how they limit the maximum surface angle that can be successfully printed using this technology. “Sag” was defined as the downwards deflection of a portion of the molten polymer print bead resulting from gravitational forces, while “droop” described this same effect but on the scale of the entire print strand. Finally, the term “shrink” was introduced to describe the contraction of the bead under the influence of surface tension.

Using an argument based on the ratio of gravitational and surface forces, we demonstrated that sag was the limiting phenomena in the printing of inclined surfaces at large scales, such as those employed in Big Area Additive Manufacturing. On the other hand, at small-scales, such as in traditional “desktop” FDM 3-D printers, we showed that shrink was the prevalent phenomena and that bead shrink leads to strand droop, which is ultimately the cause of print failure.

Two separate models were developed to predict the layer progression due to sag (large-scale FFF) and shrink (small-scale FFF). A variety of results were generated using each model by varying input parameters such as scale, layer height, surface angle, and number of perimeters. The accuracy of these results was then evaluated through comparison to equivalent experimental findings, with good conformance being demonstrated between the two.

The shrink model predictions, backed by experiment, showed that the maximum overhang angle is inversely proportional to the layer height and that the addition of a second perimeter considerably delays the onset of droop. Results for the sag model indicated that the maximum overhang angle was dependent on the rate of cooling, with faster cooling enabling the printing of steeper surfaces.

There is considerable room for future work in this field. Specifically, the sag model could be improved by incorporating more complex heat transfer mechanisms such as 2-D transient conduction and forced convection. The shrink model could be improved by adding consideration for transient flow and incorporating a more precise means of determining the surface-area-minimizing geometry. These modifications would improve the robustness of the models and provide more accurate predictions of the maximum overhang print angle in a variety of scenarios. Finally, rather than have two segmented

models which are scale-specific, a hybrid model which is scale-independent would be much more versatile and is thus worthy of further investigation.

Bibliography

- [1] (2018) Worldwide most used 3D printing technologies as of July 2018. Statista. [Online]. Available: <https://www.statista.com/statistics/756690/worldwide-most-used-3d-printing-technologies/>
- [2] *Standard Terminology for Additive Manufacturing — General Principles*, ISO/ASTM Std. 52900, 2015.
- [3] J. Jiang, X. Xu, and J. Stringer, “Support structures for additive manufacturing: A review,” *Journal of Manufacturing and Materials Processing*, vol. 2, no. 4, 2018.
- [4] C. Y. Yap, C. K. Chua, Z. L. Dong, Z. H. Liu, D. Q. Zhang, L. E. Loh, and S. L. Sing, “Review of selective laser melting: Materials and applications,” *Applied Physics Reviews*, vol. 2, no. 4, p. 041101, 2015.
- [5] M. Gan and C. Wong, “Practical support structures for selective laser melting,” *Journal of Materials Processing Technology*, vol. 238, pp. 474–484, 2016.
- [6] D. Morgan, E. Agba, and C. Hill, “Support structure development and initial results for metal powder bed fusion additive manufacturing,” *Procedia Manufacturing*, vol. 10, pp. 819–830, 2017.
- [7] P. Mercelis and J.-P. Kruth, “Residual stresses in selective laser sintering and selective laser melting,” *Rapid Prototyping Journal*, vol. 12, no. 5, pp. 254–265, 2006.

- [8] K. Arcaute, P. J. Bártolo, A. Bertsch, B. N. Chichkov, S. Corbel, and F. J. Davis, *Stereolithography: Materials, Processes and Applications*, P. J. Bártolo, Ed. Springer, 2011.
- [9] Y. Yang, J. Fuh, H. Loh, and Y. Wong, “Multi-orientational deposition to minimize support in the layered manufacturing process,” *Journal of Manufacturing Systems*, vol. 22, no. 2, pp. 116–129, 2003.
- [10] K. van Praet. (2017) First impressions of materialise e-stage for metal: An interview with process engineer hannes brenning. Materialise. [Online]. Available: <https://www.materialise.com/en/blog/interview-metal-support-generation-e-Stage>
- [11] P. Cain. (2017) Supports in 3D printing: A technology overview. 3D Hubs. [Online]. Available: <https://www.3dhubs.com/knowledge-base/supports-3d-printing-technology-overview/>
- [12] M. Zuza. (2018) How to create custom overhang supports in Meshmixer. Prusa 3D. [Online]. Available: https://blog.prusaprinters.org/how-to-create-custom-overhang-supports-in-meshmixer/#_ga=2.172171171.1051902981.1575151988-1405400857.1530040769
- [13] Simplify3D version 4.0 adds new capabilities and improved quality. Simplify3D. [Online]. Available: <https://www.simplify3d.com/simplify3d-version-4-0-adds-new-capabilities-and-improved-quality/>
- [14] P. Das, K. Mhapsekar, S. Chowdhury, R. Samant, and S. Anand, “Selection of build orientation for optimal support structures and minimum part errors in additive manufacturing,” *Computer-aided Design and Applications*, vol. 14, no. 1, pp. 1–13, 2017.

- [15] Y. an Jin, Y. He, and J. zhong Fu, “Support generation for additive manufacturing based on sliced data,” *International Journal of Advanced Manufacturing Technologies*, vol. 80, pp. 2041–2052, 2015.
- [16] G. Strano, L. Hao, R. M. Everson, and K. E. Evans, “A new approach to the design and optimisation of support structures in additive manufacturing,” *International Journal of Advanced Manufacturing Technologies*, vol. 66, pp. 1247–1254, 2013.
- [17] J. Vanek, J. Falicia, and B. Benes, “Clever support: Efficient support structure generation for digital fabrication,” *Computer Graphics Forum*, vol. 33, no. 5, pp. 117–125, 2014.
- [18] M. Leary, M. Babaee, M. Brandt, and A. Subic, “Feasible build orientations for self-supporting fused deposition manufacture: A novel approach to space-filling tessellated geometries,” *Advanced Materials Research*, vol. 633, pp. 148–168, 2013.
- [19] X. Guo, J. Zhou, Z. D. Weisheng Zhang, C. Liu, and Y. Liu, “Self-supporting structure design in additive manufacturing through explicit topology optimization,” *Computer Methods in Applied Mechanics and Engineering*, vol. 323, pp. 27–63, 2017.
- [20] J. Wang, J. Dai, K.-S. Li, J. Wang, M. Wei, and M. Pang, “Cost-effective printing of 3d objects with self-supporting property,” *The Visual Computer*, vol. 35, no. 5, pp. 639–651, 2019.
- [21] W. Wang, T. Y. Wang, Z. Yang, L. Liu, X. Tong, W. Tong, J. Deng, F. Chen, and X. Liu, “Cost-effective printing of 3d objects with skin-frame structures,” *ACM Transactions on Graphics*, vol. 32, no. 6, pp. 177:1–177:10, 2013.

- [22] R. Prévost, E. Whiting, S. Lefebvre, and O. Sorkine-Hornung, “Make it stand: balancing shapes for 3d fabrication,” *ACM Transactions on Graphics*, vol. 32, no. 4, pp. 81:1–81:10, 2013.
- [23] Y. Xie and X. Chen, “Support free interior carving for 3d printing,” *Visual Informatics*, vol. 1, no. 1, pp. 9–15, 2017.
- [24] J. Lee and K. Lee, “Block-based inner support structure generation algorithm for 3d printing using fused deposition modeling,” *The International Journal of Advanced Manufacturing Technology*, vol. 89, no. 5-8, pp. 2151–2163, 2016.
- [25] T. Lee, J. Lee, and K. Lee, “Extended block based infill generation,” *The International Journal of Advanced Manufacturing Technology*, vol. 93, no. 1-4, pp. 1415–1430, 2017.
- [26] T. Wang, Y. Liu, X. Liu, Z. Yang, D. Yan, and L. Liu, “Global stiffness structural optimization for 3d printing under unknown loads,” *Journal of Computer Graphics Techniques*, vol. 5, no. 3, pp. 18–37, 2016.
- [27] X. Zhang, Y. Xia, J. Wang, Z. Yang, C. Tu, and W. Wang, “Medial axis tree—an internal supporting structure for 3d printing,” *Computer Aided Geometric Design*, vol. 35-36, pp. 149–162, 2015.
- [28] L. Lu, A. Sharf, H. Zhao, Y. Wei, Q. Fan, X. Chen, Y. Savoye, C. Tu, D. Cohen-Or, and B. Chen, “Build-to-last: strength to weight 3D printed objects,” *ACM Transactions on Graphics*, vol. 33, no. 4, pp. 1–10, 2014.
- [29] J. Wu, N. Aage, R. Westermann, and O. Sigmund, “Infill optimization for additive manufacturing—approaching bone-like porous structures,” *IEEE Transactions on Visualization and Computer Graphics*, vol. 24, no. 2, pp. 1127–1140, 2018.

- [30] J. Wu, C. Wang, X. Zhang, and R. Westermann, “Self-supporting rhombic infill structures for additive manufacturing,” *Computer-Aided Design*, vol. 80, pp. 32–42, 2016.
- [31] E. Tyson. How to print overhangs, bridges and exceeding the 45 degree rule. RigidInk. [Online]. Available: <https://rigid.ink/blogs/news/how-to-print-overhangs-bridges-and-exceeding-the-45-rule>
- [32] B. Obudho. 3D printing overhang guide – how to 3D print overhangs. All3DP. [Online]. Available: <https://all3dp.com/2/3d-printing-overhang-how-to-master-overhangs-exceeding-45/>
- [33] Big area additive manufacturing. Cincinnati. [Online]. Available: <https://www.e-ci.com/baam>
- [34] i3 Mega S. AnyCubic. [Online]. Available: <https://www.anycubic.com/products/anycubic-i3-mega-s>
- [35] A. Alić, “Physics of 3-D Printing,” University of Ljubljana, 2017, unpublished.
- [36] S. Costa, F. Duarte, and J. Covas, “Estimation of filament temperature and adhesion development in fused deposition techniques,” *Journal of Materials Processing Technology*, vol. 245, pp. 167–179, 2017.
- [37] B. B. Shahriar, C. France, N. Valerie, C. Arthur, and G. Christian, “Toward improvement of the properties of parts manufactured by FFF (fused filament fabrication) through understanding the influence of temperature and rheological behaviour on the coalescence phenomenon,” in *Proceedings of the 20th International ESAFORM Conference on Material Forming*, Dublin, Ireland, Apr. 2017, p. 040008.
- [38] R. Comminal, M. Serdeczny, D. Pedersen, and J. Spangenberg, “Numerical modeling of the strand deposition flow in extrusion-based additive manufacturing,” *Additive Manufacturing*, vol. 20, pp. 68–76, 2018.

- [39] H. Xia, J. Lu, S. Dabiri, and G. Tryggvason, “Fully resolved numerical simulations of fused deposition modeling. part i: fluid flow,” *Rapid Prototyping Journal*, vol. 24, no. 2, pp. 463–476, 2018.
- [40] A. Verma, P. Vishnoi, V. Sukhotskiy, and E. P. Furlani, “Numerical simulation of extrusion additive manufacturing: Fused deposition modeling,” *TechConnect Briefs*, vol. 4, pp. 118 – 121, 2018.
- [41] J. D. Berry, M. J. Neeson, R. R. Dagastine, D. Y. Chan, and R. F. Tabor, “Measurement of surface and interfacial tension using pendant drop tensiometry,” *Journal of Colloid and Interface Science*, vol. 454, pp. 226–237, 2015.
- [42] J. D. 3D printing: The future of construction. [Online]. Available: <https://www.3dnatives.com/en/3d-printing-construction-310120184/>
- [43] B. Ludlum. 3D printing infill vs shell. [Online]. Available: <https://mycrazygoodlife.com/3d-printing-infill-vs-shell/>
- [44] D. W. Mackowski, “Conduction Heat Transfer Notes for MECH 7210,” Mechanical Engineering Department Auburn University, 2015, unpublished.
- [45] D. Ferri, A. Perolo, and M. Nodari, “Cross-WLF parameters to predict rheological properties of polylactic acid,” *Annual Transactions of the Nordic Rheology Society*, vol. 25, pp. 419 – 426, 2017.
- [46] “Moldflow material testing report: Natureworks PLA,” Moldflow Plastic Labs, Tech. Rep., 2007. [Online]. Available: https://www.natureworkslc.com/~media/TechnicalResources/Properties_Documents/PropertiesDocument_7000DMoldFlowReport_pdf.pdf
- [47] C. Ajinjeru, V. Kishore, P. Liu, A. A. Hassen, J. Lindahl, V. Kunc, and C. Duty, “Rheological evaluation of high temperature polymers to identify successful extrusion parameters,” in *Proceedings of the 28th Annual*

International Solid Freeform Fabrication Symposium, Austin, TX, Aug.
2017, pp. 485–494.